Time-of-Flight Investigation of Charge Carrier Mobilities in Oligoacene Single Crystals

A DISSERTATION
SUBMITTED TO THE FACULTY OF THE GRADUATE SCHOOL
OF THE UNIVERSITY OF MINNESOTA
BY

Russell L. Lidberg

IN PARTIAL FULFILLMENT OF THE REQUIREMENTS
FOR THE DEGREE OF
DOCTOR OF PHILOSOPHY

C. Daniel Frisbie, Advisor

August 2017

Acknowledgements

I would like to take this opportunity to thank everyone that has helped me along the way over the many years. I have interacted with many fine individuals in my career and to list them all here would be overwhelming. So, everyone, please accept my sincere thank you.

The work presented here was done while I was with St. Cloud State University. Over that time, I have interacted with a number of faculty and staff, and I would like to thank them all. During my time at St. Cloud State I was fortunate to work with a number of undergraduate students providing them with research activities that hopefully will help them along their career paths. Several students were involved in different ways in this work and I would like to acknowledge them. The following list of students (in alphabetical order) spent time in the lab working on this project: Andrew Davies, Matthew L. Gesmundo, Joseph Harter, Neale Haugen, Lucas Jedlicka, Luke Johnstone, Desiree Lee, Justin Paulsen, Tom Pundsack, Aaron Schulzetenberg and Brandon Smith. If I have overlooked anyone please accept my apologies.

I would like to also thank my advisor, C. Daniel Frisbie, for his patience and support as we put this project together and have seen it to this point.

Finally, I would thank my wife, Faye, and my children, Bradley and Jessica, who have put up with me over the years as I sometimes became distracted from family life when my thoughts would drift into research.

Abstract

Organic semiconductors remain an active area of research due to their unique mechanical and opto-electronic properties. The charge transport properties of organic semiconductors are dependent on their molecular packing structures. A fundamental understanding of the charge transport and device physics on a microscopic scale remains a central focus of discussion. Models and theories have been based on the understanding derived from inorganic systems, but these tend not to hold for organic semiconductors. Single crystals of small conjugated oligoacenes, with high chemical purity and molecular structural order, can be model systems in the study of the relationship between molecular packing and carrier charge transport. The ability to probe intrinsic charge transport, not influenced by environmental factors or measurement techniques, plays a fundamental role in gaining a deeper understanding of the factors affecting charge transport. Time of flight (TOF) is an experimental technique used for charge carrier mobility studies that minimizes the external factors affecting charge transport. TOF also has the potential to study both bulk (vertical) and surface (lateral) charge carrier transport in organic semiconductors.

This work reports the charge carrier mobility in single crystals of tetracene and rubrene using vertical and lateral field TOF (LFTOF). TOF instrumentation was designed and constructed. Room temperature vertical TOF hole mobility results in the **c**-direction for tetracene single crystals were acquired as a function of electric field (μ_c

≈ 1.3 cm^2/Vs at 296 K). Bulk TOF hole charge carrier in rubrene single crystal as a function of temperature and electric field were acquired with an average value of 0.29 cm^2/Vs at 296 K increasing to 0.70 cm^2/Vs at 180 K and demonstrated an inverse power law temperature dependence, 'band-like' transport, in the **c**-axis direction. The use of LFTOF to study transport on the surface of single crystal organic semiconductors was demonstrated. LFTOF hole mobilities of 0.8 cm^2/Vs at 296 K were in the range of reported field effect transistor mobility results. An overview of organic semiconductors and traditional transport models along with emerging transport models for organic semiconductors is presented.

Table of Contents

List of Tables

List of Figures

List of Abbreviations

FET	Field Effect Transistor
HOMO	Highest Occupied Molecular Orbital
INDO	Intermediate Neglect of Differential Overlap
LFTOF	Lateral Field Time of Flight
LUMO	Lowest Unoccupied Molecular Orbital
NA	Numerical Aperture
OFET	Organic Field Effect Transistor
PVT	Physical Vapor Transport
RC	Resistance Capacitance
TOF	Time of Flight
XRD	X-ray Diffraction

Chapter 1

Introduction

1.1 Motivation of the Thesis

Electronic and electrooptical materials based on organic molecules are undergoing intensive study ranging from basic materials science to possible technological applications.[1-3] This interest has in part stemmed from the desire to provide a new class of materials that can afford properties that are not realizable in traditional Si-based devices. Properties such as lower cost, simpler processing techniques, sustainability (synthesized instead of mined, recyclable and potentially biodegradable), flexible device designs, biocompatibility and energy efficiency have opened new doors for these materials.[4-9] The lower cost of material synthesis and device manufacturing has the potential to provide advanced technology to remote and impoverished portions of the globe. Due to processing and mechanical advantages and the ability to chemically tune their electronic and optical properties, the use of organic materials in future devices has the potential to replace or complement their inorganic counterparts. Design of organic materials with electrical properties that rival or surpass those of inorganics, is ushering in a new generation of electronic and optical devices.

The areas of use are endless and include communications, sensing, biomedical and energy production. These molecular organic semiconductor materials have found a wide range of device applications with the major focus of research being in the development of organic field-effect transistors (OFETs),[10-14] organic photovoltaic devices (OPVs)[15-18] and organic light emitting diodes (OLEDS)[19-21].

There is a strong interest to obtain a more complete understanding of charge carrier transport in organic semiconductor materials. Single crystals of small oligoacenes (tetracene, rubrene) make a perfect testbed to study these transport properties due to their highly ordered structure and purity.[22-24] The technique used in measuring the mobility is also an issue in the examination of mobility to study carrier transport properties. It is preferred to look at intrinsic (not affected by external conditions) mobility. Time of Flight (TOF) is a technique that allows for the study of these materials with minimal perturbation of the intrinsic transport properties of the material.[25] The main goals of this thesis deal with investigating the charge carrier mobilities in single crystal oligoacenes using TOF techniques. Specific goals of this work include:

1) Design, construct and demonstrate instrumentation capable of vertical (crystal bulk) TOF and lateral (crystal surface) TOF charge carrier mobility measurements including low temperature bulk mobilities.

2) Investigate low temperature TOF mobilities in oligoacene single crystals to help advance the understanding of transport theory in single crystal semiconductor materials.

Study the bulk (**c**-axis) mobility of rubrene single crystals as a function of temperature, below room temperature, using TOF.

3) Examine the use of lateral field TOF in determining the intrinsic charge carrier mobilities on the surface of oligoacene single crystals to compare with field effect techniques.

1.2 Synopsis of Thesis

Chapter 2 introduces the principles of the electronic properties of conjugated organic semiconductors and the basic concepts of charge carrier motion in these materials.

Chapter 3 provides a theoretical overview of classical charge transport including a discussion of new thoughts on charge transport in ordered organic semiconductor materials.

Chapter 4 reviews experimental methods used for determining charge carrier mobilities that are relevant to this work.

Chapter 5 covers experimental techniques used in this work along with the design and construction of the TOF instrumentation.

Chapter 6 presents experimental results for vertical and lateral TOF measurements. Portions of Chapter 6 were published as: Pundsack, T.J.; Haugen, N.O.;

Johnstone, L.R.; Frisbie, C.D.; Lidberg, R.L. Temperature Dependent c-Axis Mobilities in Rubrene Single Crystals Determined by Time-of-Flight. *Appl. Phys. Lett.* **2015**, *106*, 113301.

Chapter 2

Organic Semiconductors

This chapter introduces the principles of the electronic properties of conjugated organic semiconductors and the basic concepts of charge carrier motion in these materials.

2.1 Organic Electronic Materials – Introduction

Organic π-conjugated materials have taken a major role in the study of organic semiconductors due to the fact that the properties of these materials such as band gap, redox potentials and charge transport properties can be tuned to control device performance.[26-28] The design and implementation of these organic materials requires a basic understanding of their physical properties. The transport of the charge carriers (electrons or holes) is important to device performance. For instance, the carrier transport can affect the switching speed and the operational frequency in transistors. In solar cells, the carrier transport can affect the recombination lifetime of charge carriers thus significantly influencing the efficiency of the device. In addition, these materials

can be processed by simple solvent processing techniques and therefore, provide for light weight, potentially low cost, thin film, large-area and flexible device fabrication. With all the promise of these materials, there are issues that need to be addressed to increase their performance and integration into daily use devices. Some of these issues include low charge carrier mobility, electronic and optical stability and incompatibility with classical semiconductor processing techniques.

To address underlying issues associated with organic semiconductor materials and improve device performance a deeper understanding of the fundamental properties of these materials is needed. This task is complicated by the large assortment of representative molecular organic semiconductor materials available as well as the structural packing in the solid state, amorphous vs crystalline. One of the most basic issues is to gain a better understanding of the factors governing charge carrier transport. Several intrinsic factors are involved in defining transport including crystal packing, chemical impurities, structural defects, and thermal disorder.[29-30] The ability to control these factors allows for the understanding and thus design of materials and devices with improved performance. The use of single crystals materials with high purity and structural ordering, provides an avenue to control and minimize these factors. Single crystals have become an important tool in the development of organic semiconductor materials.

2.2 Electronic Properties of Organic Semiconductors

While there are a wide range of organic based molecular systems that are being studied for the use in organic electronic and electrooptic devices, much work has focused on small conjugated molecules and conjugated polymers.[2, 13, 31-34] Single crystals of small molecular species such as the oligoacenes (tetracene, pentacene, and rubrene) have been studied (Figure 2.1).[35-40] These studies have looked at the fundamental physical parameters that govern charge transport as well as their potential use in devices. One overlapping characteristic of these molecules is the presence of a conjugated electron system. Below we discuss the origin and properties of conjugation in organic molecules.

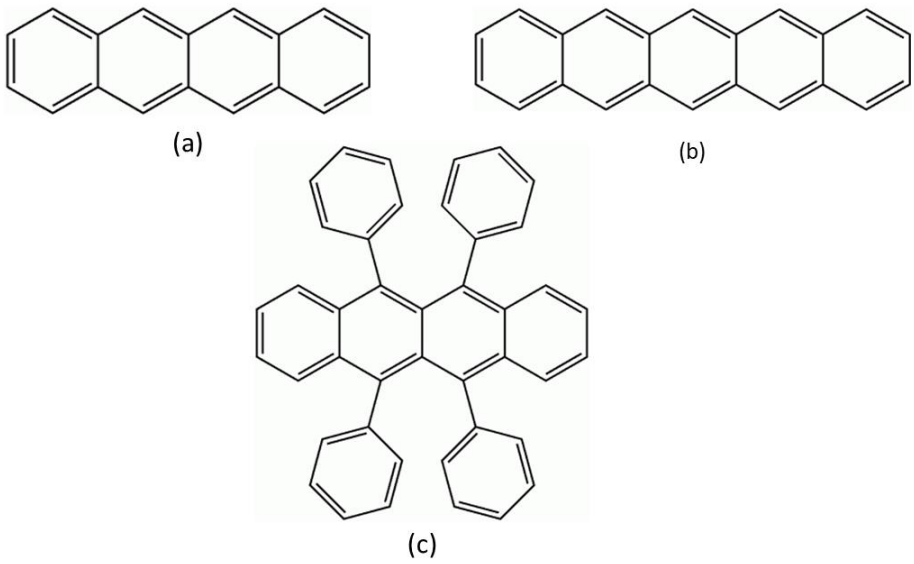

Figure 2.1: Structures of organic semiconducting oligoacenes: (a) tetracene, (b) pentacene, (c) rubrene.

2.2.1 Conduction in Conjugated Molecules

Conjugated π- electron molecular systems define the dominant feature of organic semiconductors and are the main materials of interest and are the focus of this study. Conjugated systems in organic molecules are a result of covalently bonded carbon atoms, with alternating single and double bonds.[41-42] In a bonded carbon atom, the electronic configuration is $1s^2 2s 2p^3$. Carbon-carbon double bonds are a result of sp^2 hybridization of the carbon orbitals creating 3 degenerate σ bonds with strongly localized electron density. The 3 σ bonds are formed in the plane of the molecule from the 2s and two 2p orbitals. The sp^2 hybridized atomic orbitals form from the overlap of atomic orbitals of adjacent carbon atoms resulting in strong σ-bonds. The remaining unhybridized p_z orbital is perpendicular to the plane of the σ bonds. The p_z orbitals of adjacent carbon atoms overlap and form a π bond which is a weaker bond than the σ bonds. The electron density of the π bond is delocalized and extends above and below the plane of the bond between the carbon atoms (Figure 2.2).

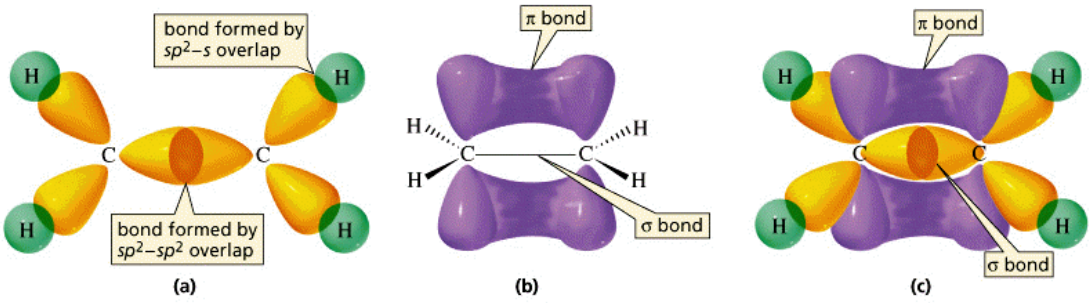

Figure 2.2: Sigma and pi bonding in ethene.[43]

In a multi conjugated system, such as benzene, these delocalized π electrons are free to move through the entire molecule.

This π bond formation results in π bonding orbitals known as the highest occupied molecular orbital (HOMO) and π* antibonding orbitals known as lowest unoccupied molecular orbital (LUMO) (Figure 2.3).[44-45]

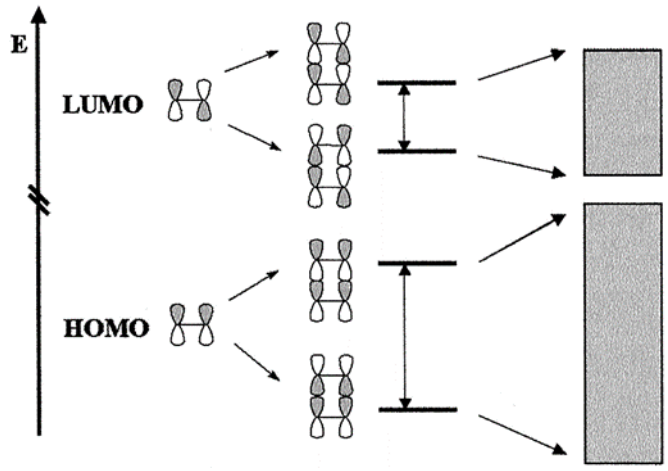

Figure 2.3: Illustration of the bonding–antibonding interactions between the HOMO/LUMO levels of two ethylene molecules in a cofacial configuration. Right side: valence (lower band) and conduction (upper band) bands formed when a large number of stacked molecules interact.[44] Reprinted with permission. Copyright 2002 National Academy of Sciences, U.S.A.

When the molecule is in the ground state the bonding orbitals are filled by two electrons of opposite spin up to the energy level of the HOMO while the antibonding orbitals at and above the energy level of the LUMO are empty. It is the separation energy of the HOMO and LUMO that defines the energy bandgap of the molecular

semiconductor. An electron can be excited from the HOMO to the LUMO level by the absorption of light with energy equal to or greater than the energy separation of the two levels. This excitation results in a neutral excited state in the molecule.

As two isolated conjugated molecules are brought together, the π orbital overlap and the energy levels split into two different levels. As N molecules are brought together in the solid state the levels split into N different levels which form two continuous bands, the conduction band CB and the valence band VB separated by the bandgap,[46] as seen on the right side of Figure 2.3. The width of the bandgap can be controlled by tuning the molecules planarity, aromaticity, bond length pattern and the attached electron withdrawing or donating groups.[47] As the interaction between π-orbitals increases, typically when the inter-atomic distance d, decreases, the splitting and the thus the bandwidth (splitting) increases as shown in Figure 2.4. This orbital (wavefunction) overlap is a central feature in charge carrier transport providing a path for the delocalization of the carrier throughout the material. As the bandwidth increases the carrier mobility tends to increase. The overlap can be quantized as the transfer integral (which can be noted as t or *J* in the literature) which is related, using a tight binding model, to the bandwidth (BW)[48] as

$$BW = 4t. \tag{2.1}$$

The transfer integral is a leading parameter in describing the carrier mobility. The degree of splitting of the HOMO (LUMO) and thus the transfer integral related to each orbital plays a major role in defining the magnitude of the hole (electron) mobility.

It can then be implied that anything that could affect the position of a molecular orbital in relation a neighboring orbital, (e.g., temperature, vibrational motion), would affect the magnitude of the transfer integral.[29]

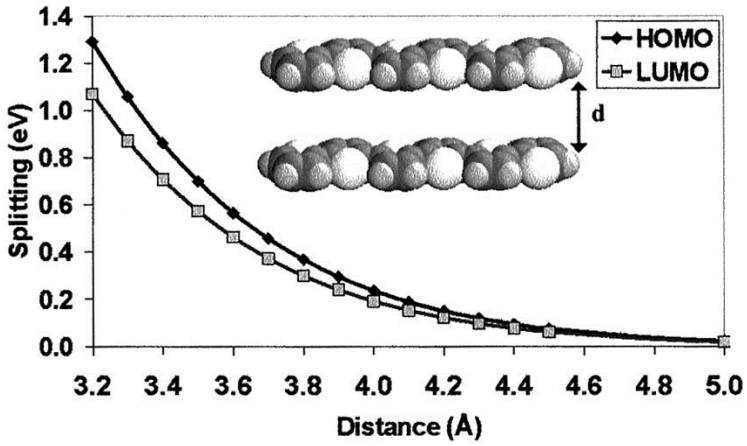

Figure 2.4: Evolution of the electronic splitting of the HOMO and LUMO levels in a cofacial dimer of two sexithienyl molecules as a function of the intermolecular separation. Calculated using the INDO - Intermediate Neglect of Differential Overlap - method.[44] Reprinted with permission. Copyright 2002 National Academy of Sciences, U.S.A. (BredasPNAS2002)

2.2.2 Classical Carrier Motion

Charge carrier motion in a material can be affected by thermal motion, carrier diffusion and carrier drift.[49-50] If a free carrier is available in thermal equilibrium with no applied electric field, carriers are in motion undergoing collisions with the vibrating molecular structure with random Brownian motion. The carriers may interact with

phonon scattering events and possibly electrostatically with ionized impurities or with each other. These events can be characterized from this thermal motion by a mean free time between collisions, τ_m (s). In between collisions, carriers can acquire a thermal velocity, v_{th} (cm/s). They have a characteristic length of motion referred to as the mean free path, λ, where $\lambda = v_{th}\tau_m$. Since this thermal movement is random and is not affected by an external field, the tendency is for the carrier distribution to remain constant, they essentially go nowhere.

The movement of charge carriers in a semiconductor material can be defined as either a diffusion process or a drift process. In a diffusion process, charge carriers tend to move from areas of higher concentration to areas of lower concentration. This movement is in response to the concentration gradient and tends to move towards a concentration equilibrium. In semiconductors, this movement of carriers from a region of higher concentration to lower concentration results in a diffusion current.

This diffusion process can be defined by the diffusion relationship given by Fick's first law where the diffusion flux, F, is proportional to the carrier concentration gradient, dn/dx. The flux is the number of particles crossing a unit area per unit time ($cm^{-2} \cdot s^{-1}$). The carrier flux, in one dimension, can be written as

$$F = -D\frac{dn}{dx} \tag{2.2}$$

D is the carrier (electron or hole) diffusion constant with units of (cm^2/s) and measures the ease of carrier diffusion in response to a concentration gradient. The diffusion

coefficient is affected by molecular motion, grain boundaries and trap states. The resulting diffusion current, J_{diff}, can be expressed as the charge times the flux:

$$J_{diff} = \pm qD\frac{dn}{dx} \tag{2.3}$$

where q is the elementary charge (1.6×10^{-19} Coulomb) and +q or –q refers to the charge on the hole or electron, respectively.

Drift transport occurs when an electric field, E(V/cm), is applied to a semiconductor resulting in a net force, F = ±qE, on the carriers. Between collisions, the carriers accelerate in the direction of the applied field with a velocity of $v(t) = (-q\tau_m/m^*)E$, for electrons and $v(t) = (q\tau_m/m^*_p)E$, for holes, where m^*_n and m^*_p are the effective masses (discussed below) of the electron and hole, respectively. Taking into account the scattering of the carrier and the mean free time, τ_m, the average drift velocity in the direction of the field, with units of cm/s is given by

$$v_{drift} = \left(\pm\frac{q\tau_m}{m^*_{n,p}}\right)E. \tag{2.4}$$

The mobility, μ, can be considered as a measure of the ease of carrier drift and is defined as the average velocity gained per unit field, $v_{drift}/E = (q/m^*)\tau_m$:

$$\mu_{n,p} = q\frac{\tau_m}{m^*_{n,p}} \quad \left(\frac{cm^2}{Vs}\right) \tag{2.5}$$

and the drift velocities $v_{driftn} = -\mu_n E$ for electrons and $v_{driftp} = \mu_p E$ for holes. The drift current, J_{drift} can then be written as

$$J_{drift} = qNv_{drift} = qN\mu E. \quad (2.6)$$

The drift and diffusion of the carriers can be related to each other through the Einstein relation. The total current, J_{tot} can be written as a sum of the drift and diffusion components.

$$J_{tot} = qN\mu E = qD\frac{dn}{dx} \quad (2.7)$$

Under equilibrium conditions, where the drift and diffusion currents cancel each other, $J_{tot} = 0$, it can be shown that

$$D = \frac{kT}{q}\mu \quad (2.8)$$

This is the Einstein relation that is widely used in carrier transport in semiconductors at low carrier concentrations. The drift mobility, μ, from charge hopping is then evaluated from the Einstein relation, leading to the bulk (isotropic) mobility of the material.

$$\mu = \left(\frac{q}{k_B T}\right) D. \quad (2.9)$$

2.2.3 Factors Affecting Mobility

A characteristic feature of organic semiconductor crystals is the anisotropic molecular packing in the crystals three-dimensional structure. This anisotropic packing

results in different degrees of electronic coupling in different directions in the crystal.[51] Figure 2.5 shows the packing of pentacene and rubrene crystals and varying transfer integrals.

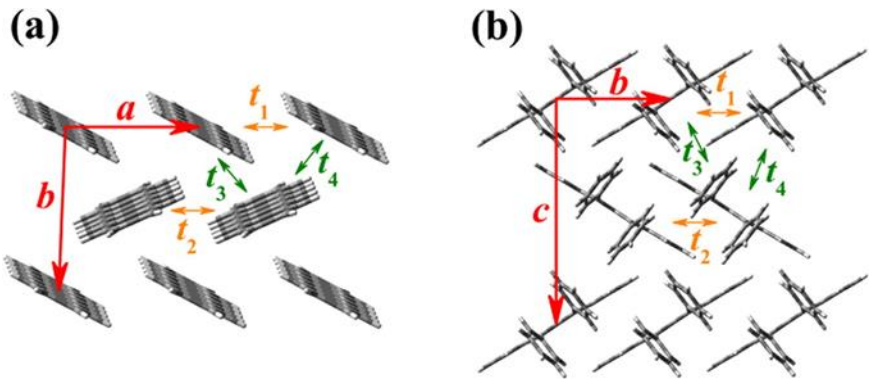

Figure 2.5: Crystal structure and largest transfer integrals for a) pentacene and b) rubrene single crystals**.** The t directions represent nonequivalent transfer integrals.[52] Reprinted with permission. Copyright 2012 American Chemical Society**.**

In addition, the anisotropic molecular packing results in different degrees of thermal expansion in different crystal directions. Due to the weak van der Waals interactions in the crystal the resulting forces holding the crystal together are different along different crystal axes. This anisotropic crystal expansion with a change in temperature has been shown to occur in a rubrene single crystal. The single crystal x-ray diffraction results showed a 2.157% volume thermal expansion of the crystal from 100 K to 300 K. The results also showed the thermal expansion was anisotropic for the three crystallographic directions ($\Delta a = 0.410\%$, $\Delta b = 0.320\%$, $\Delta c = 1.562\%$) with the largest change occurring along the weakest bonding c-axis as shown in Figure 2.6.[53]

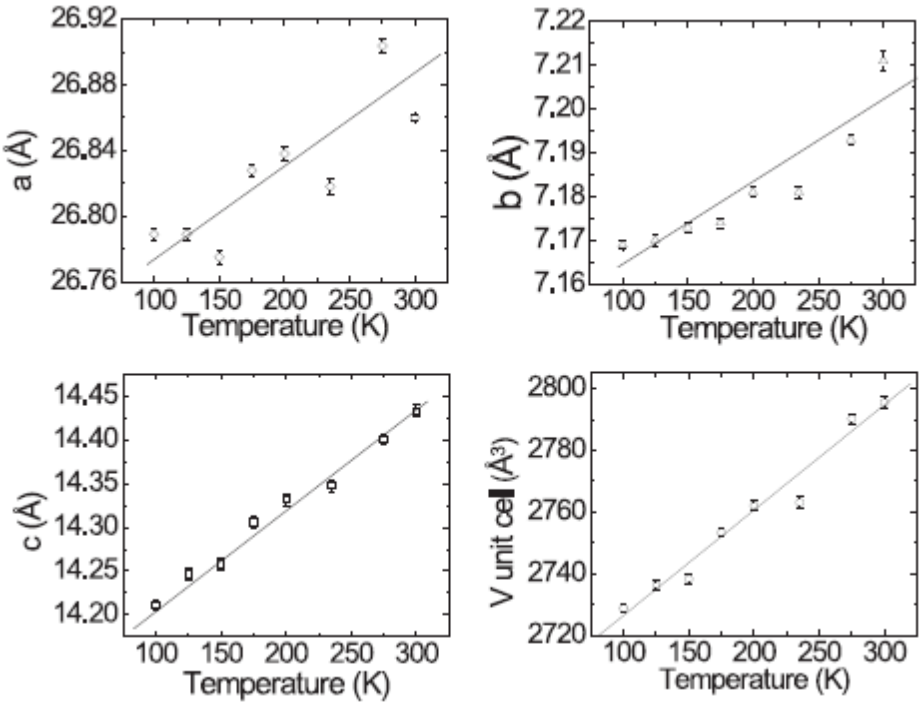

Figure 2.6: Lattice parameters **a**, **b** and **c**, and unit cell volume V versus temperature for rubrene single crystals**.** The lines are guides for the eyes.[53] Reproduced with permission of the International Union of Crystallography.

This variability and anisotropic coupling results in nonequivalent band structure in different crystal directions and as will be shown below, this changing band structure results in changes in the effective mass of the carrier and thus the carrier mobility.

The transport of carriers in a semiconductor crystal is a result of the applied field but is also affected by the crystal potential due to the lattice atoms (nucleus and core electrons). In a one-dimensional crystal the crystal potential, V(x), varies due to the position of the lattice atoms (molecules). For a crystal that has a constant repeating lattice, the periodicity in the crystal potential can be written as

$$V(x) = V(x + a) \tag{2.10}$$

where, a, represents the lattice constant in the x-direction. The behavior of the carrier in a crystal can be observed by solving the Schrodinger equation (1D in this case)

$$\left[-\frac{\hbar^2}{2m}\frac{d^2}{dx^2} + V(x)\right]\Psi(x) = E\Psi(x) \tag{2.11}$$

where, Ψ(x), is the state function and, E, is the energy of the carrier. The Bloch theorem states that the solution of the Schrodinger equation for a periodic potential can be given by the Bloch function

$$\Psi_k(x) = u_k(\mathrm{x})\exp(i\mathbf{k}\mathrm{x}) \tag{2.12}$$

where

$$u_k(x) = u_k(x + a) \tag{2.13}$$

is the periodic condition. The movement of the carrier can be defined by the wave vector, **k**, with a deBroglie wavelength of $\lambda = 2\pi/k$. It can be related to the carrier's momentum, p, by the deBroglie relation, $\lambda = h/p$ as $\mathbf{p} = \hbar\mathbf{k}$ and is also referred to as the crystal momentum.[54-55]

We can solve for the energy of the carrier as a function of the wave vector. By substituting the Bloch function (Equation 2.12) into the Schrodinger equation and applying the periodic boundary conditions (Equation 2.13) we can solve for the energy eigenvalue, E(k) and the eigenfunction, u_k. Since this is an eigenvalue equation it can yield a number of solutions each giving discrete energies as a function of **k** which can

be labeled as a discrete range of energies, $E_{1\mathbf{k}}$, $E_{2\mathbf{k}}$ …. These energies vary as **k** varies, over a given range and leads to specific energy bands. Figure 2.7 shows a range of allowed energy bands separated by bandgaps, forbidden energies that cannot be occupied by the carriers. Since **k** is a vector quantity, the plots of the energy bands are specific for given direction in space. A plot of E(**k**) in a different direction would possibly yield an energy band with a different shape possibly due to the difference in crystal potential in that direction.

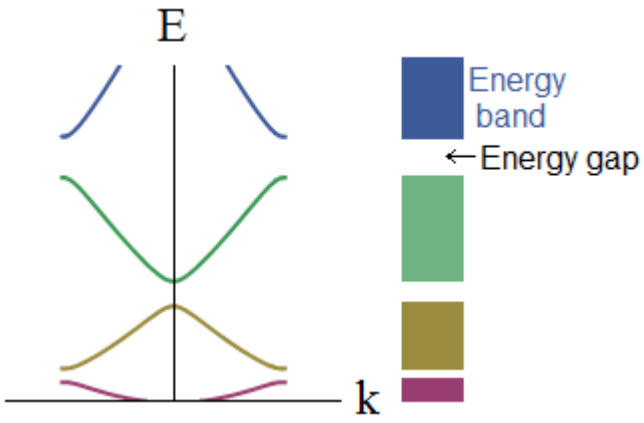

Figure 2.7: Relationship of energy vs **k** resulting in allowed energy bands and forbidden bandgaps.[56]

It has been shown that the charge carrier mobility is related to the effective mass of the carrier. A carrier in a periodic potential is accelerated relative to the lattice in an applied electric field as if the mass of the electron were equal to an effective mass. The complete set of energy levels of a crystal can be described in terms of the wave vector, **k**. The energy levels of a carrier in a periodic potential is then described in terms of a

set of wave functions, E(**k**), the dispersion relation, energy as a function of wave vector. These wave functions define the band structure of the solid. If we take a simple parabolic band expression for the energy where

$$E(k) = \frac{\hbar^2 k^2}{2m^*}. \tag{2.14}$$

According to the approach known for the parabolic bands in inorganic semiconductors the effective mass, m*, depends on the inverse of the band dispersion. Taking the second derivative, we get

$$\frac{1}{m^*} = \frac{1}{\hbar^2}\frac{d^2E}{dk^2} \tag{2.15}$$

which gives the effective mass in terms of the curvature of the energy bands. The charge carrier mobility is inversely proportional to the effective mass. An energy band with a large curvature/large bandwidth, results in a small effective mass, and the carriers are easier to accelerate, whereas for small curvature/little dispersion the effective mass is higher, the carriers are harder to accelerate.[55, 57] Figure 2.8 shows the band structure calculations for rubrene in different crystallographic directions showing different electronic coupling throughout the crystal structure which leads to variations in mobility in different crystal directions.[52] Figure 2.8 also demonstrates the changes in the band structure as a function of temperature. The valence bandwidth in the Γ→Y direction narrows from 493 meV (100 K) to 445 meV (296 K). This difference in mobilities for

different crystal direction was observed in FET mobility measurements in the **a** and **b** crystal directions in rubrene with higher mobility observed in the **b** direction as shown in Figure 2.9.[58] The relationship between temperature and FET mobility along the **a** and **b** directions is shown in Figure 2.10.

Of interest in this discussion, is the increase in mobility with decreasing temperature when the crystal is cooled from 296 K to 175 K. This is a signature of bandlike transport which implies the charge carrier is delocalized over several molecular sites. This observation of bandlike transport in organic semiconductors along with the additional observation of thermally activated hopping transport has lead researchers to look at carrier transport in terms of traditional transport models based on inorganic materials. As will be discussed in Chapter 3, these models do not fully explain transport in single crystal material and alternative approaches are now coming to the forefront.

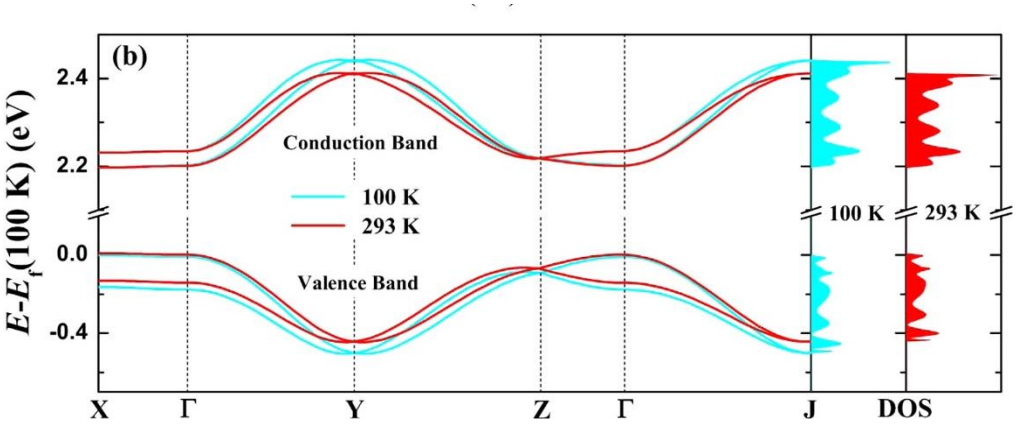

Figure 2.8: Band structure and density of states (DOS) for a rubrene crystal at 100K and 296K. Coupling in the **b** direction of the unit cell is represented by the Γ to Y=1/4 (**a***, **b***) direction in the Brillouin zone of the primitive cell.[52] Reprinted with permission. Copyright 2012 American Chemical Society.

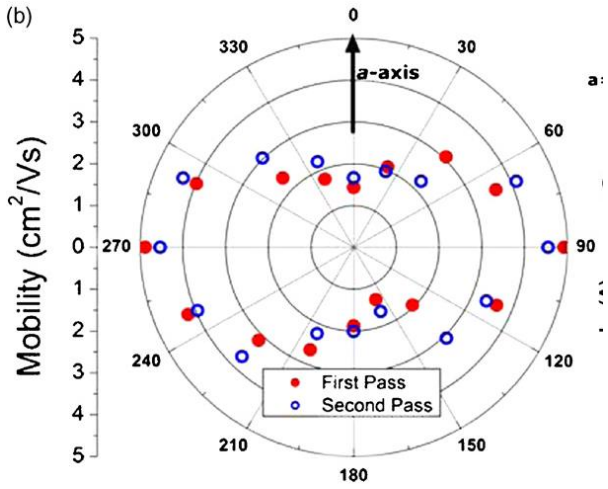

Figure 2.9: Measured effective rubrene single crystal field-effect mobility as a function of source–drain orientation in the **a**-axis (vertical 0-90 degrees direction) and **b**-axis (horizontal 90 to 270 direction).[58] Reprinted with permission. Copyright 2007 Elsevier.

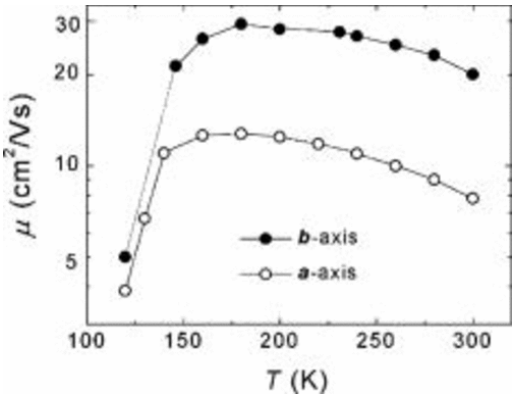

Figure 2.10: The temperature dependence of the field-effect mobility measured along the **a** and **b** axes of rubrene crystals.[59] Reprinted with permission. Copyright 2006 American Physical Society.

2.3 Crystals Examined in this Work

Single crystals of tetracene and rubrene were the focus of this work. Their crystal structures and crystallographic parameters are given below. Both tetracene and rubrene single crystals grown by physical vapor transport (discussed in Chapter 5), grow as flat platelets with the large facet corresponding to the **a**-**b** surface plane and the **c**-axis perpendicular to the crystal surface.

2.3.1 Tetracene

Tetracene crystalizes in a herringbone arrangement in the triclinic packing motif ($P\bar{1}$ spacegroup). The lattice parameters are: **a** = 6.075 Å, **b** = 7.93 Å, **c** = 13.46 Å. The crystal structure of tetracene is shown in Figure 2.11.

2.3.2 Rubrene

Rubrene single crystals grown by physical vapor transport has a orthorhombic packing motif (*Cmca* space group). The lattice parameters are **a** = 7.18 Å, **b** = 14.43 Å and **c** = 26.90 Å. The crystal structure of rubrene is shown in Figure 2.12.

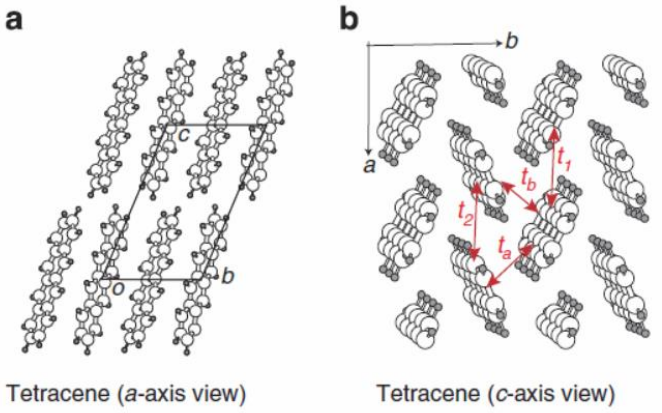

Figure 2.11: Crystal structure of tetracene. The tetracene crystal structure seen from (a) the **a**-axis and (b) the **c**-axis. The in-plane transfer paths are indicated with arrows.[60] Reprinted by permission. Copyright 2014 Macmillan Publishers Ltd.

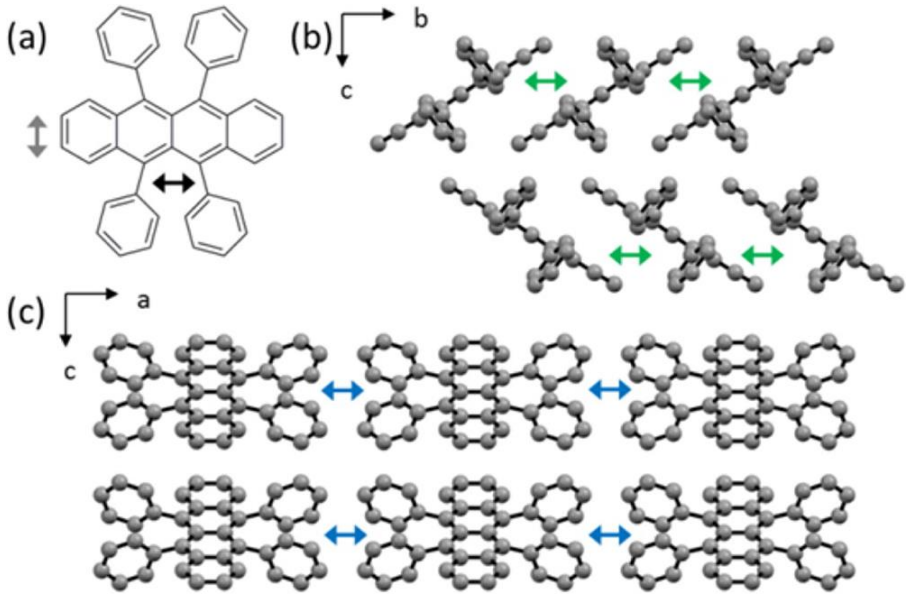

Figure 2.12: Crystal structure of rubrene (a) Molecular structure of rubrene (**1**); black arrow indicates molecular long-axis, and gray arrow indicates molecular short-axis of the tetracene backbone (core). (b) Crystal structure in the ***b*–*c*** plane; green arrows indicate direction of π-stacks between tetracene backbones. (c) Crystal structure in the ***a*–*c*** plane; blue arrows indicate direction of layers (interlayer distance). Hydrogen atoms omitted for clarity.[28] Reprinted with permission. Copyright 2013 American Chemical Society.

Chapter 3

Charge Transport in Organic Semiconductors

The mechanism of charge transport in single crystal organic semiconductors has been evolving since the early efforts to explain intrinsic charge transport in molecular crystals. Attempts at understanding this transport initially used established models developed for wide band inorganic semiconductor materials. Models such as the semiclassical Boltzmann theory[61], Marcus hopping theory[62-63] and Holstein small polaron theory[64-65], developed by way of inorganic semiconductors, have been used to try to describe transport in organic semiconductors. These discussions have been bounded by traditional delocalized band-like transport at low temperatures, similar to the behavior in inorganic semiconductors and hopping transport defined by localized states at higher temperatures, similar to disordered materials. Band-like transport at low temperatures in ordered molecular systems, is a result of the strong electronic coupling between adjacent molecules with the charge carrier wavefunction becoming delocalized over adjacent molecules. The carrier mobility thus increases with decreasing temperature as a result of fewer phonon scattering events, similar to inorganic

semiconductors.[66-67] Hopping transport occurs when there is an increase in spatial or energetic disorder and the charge carrier wavefunction becomes localized on a single molecule, the basis for small polaron transport. Carrier hopping can be thermally activated and the carrier can move from site to site if there is enough energy to overcome the reaction coordinate barrier. The carrier mobility then increases with increasing temperature.[29, 68]

The charge transport mechanism for molecular crystals at around room temperature is less defined due to a crossover region from band-like Bloch states to hopping transport.[69-70] As a result, the traditional approaches applied did not completely explain charge transport in ordered organic systems and new approaches have been proposed. An approach that has recently been gaining favor is one of charge localization as a result of dynamic disorder in the crystal.[67, 71-72] This molecular disorder is a result of thermal molecular motion that disrupts the molecular lattice resulting in large fluctuations around the equilibrium structure which in turn cause fluctuations in the electronic coupling between molecules disrupting the 'band-like' transport. These large thermal molecular motions can be explained due to the weak intermolecular van der Waals forces that hold organic solids together. These molecular fluctuations are characterized by slow low frequency modes resulting from weak restoring forces and the large molecular masses of the crystal. This dynamic disorder holds in directions of high electronic coupling such as in the **ab** plane of rubrene. In directions which low or non-existent coupling, the **c**-direction in rubrene, the dynamic disorder explanation is minimized and a model based on incoherent hooping has been proposed.[73]

The following discussion will cover the basic microscopic parameters that influence carrier transport in ordered organic molecular crystals. The models associated with the varying transport regimes will be briefly covered and limitations of such discussed. The merits of the transient localization approach will then be covered.

3.1 Traditional Approach to Charge Transport

The charge transport in organic semiconductors can be described by a number of microscopic parameters which involve electronic and phononic states along with electron-phonon coupling processes. Most models start with a 1-D minimalistic approach and assume only bulk conductance with no static disorder. Interactions between charge carriers and the applied electric field are routinely not included in charge transport models. Carrier-carrier and carrier-field interactions are ignored. The Hamiltonian relating the electrons, phonons and coupling can be written as:[74-75]

$$H = H_{el}^{0} + V_{el} + H_{ph}^{0} + V_{el-ph}^{local} + V_{el-ph}^{nonlocal} \tag{3.1}$$

where:

$$H_{el}^{0} + V_{el} = \sum_{j} \varepsilon_j a_j^{+} a_j + \sum_{ij} J_{ij} a_i^{+} a_j \tag{3.2}$$

$$H_{ph}^{0} = \sum_{\vec{q}s} \hbar\omega_{\vec{q}s}\left(b_{\vec{q}s}^{+} b_{\vec{q}s} + \frac{1}{2} \right) \tag{3.3}$$

$$V_{el-ph}^{local} = \sum_{\vec{q}s} \sum_{j} \hbar\omega_{\vec{q}s}\, g_{jj,\vec{q}s}\, (b_{\vec{q}s}^{+} + b_{-\vec{q}s}) a_j^{+} a_j \tag{3.4}$$

$$V_{el-ph}^{nonlocal} = \sum_{\vec{q}s} \sum_{i \neq j} \hbar\omega_{\vec{q}s}\, g_{ij,\vec{q}s}\, (b_{\vec{q}s}^{+} + b_{-\vec{q}s}) a_i^{+} \tag{3.5}$$

H^0_{el} and H^0_{ph} define the electronic and nuclear Hamiltonians of the non-interacting molecules, respectively. ε_j is the electronic site energy. a^+_j and a_j are the creation and annihilation operators for a charge carrier on site j and $b_{\vec{q}s}^{+}$ and $b_{\vec{q}s}$ are the creation and annihilation operators for a phonon with a wavevector $\vec{q}$, polarization index s and a frequency $\omega_{\vec{q}s}$. V_{el} is the electronic coupling term and represents the interaction of each localized state with its neighbors where J is the electronic coupling or overlap integral between states localized on adjacent molecules. $V^{local}_{el\text{-}ph}$ is the local electron-phonon coupling (Holstein type model[64-65]) and accounts for the modulation of the site energy, ε_j, due to internal or intramolecular vibrations. $V^{nonlocal}_{el\text{-}ph}$ is the nonlocal electron phonon coupling (Peierls type model[76]) and affects the electronic coupling integral which is defined by the orientation and distance between adjacent molecules. $g_{ij,\vec{q}s}$ and $g_{jj,\vec{q}s}$ are the nonlocal and local electron-phonon coupling constants, respectively.

These coupling constants measure the interaction between the intermolecular and intramolecular vibrations and the electrons.

3.1.1 Site Energy

The site energy, ε_j, is the energy associated with a charge (electron or hole) localized on a given molecular crystal site and is the difference between the energy of the neutral site and the energy of the charged site.[77] The energy of the charged site is determined by the electron affinity for an electron and the ionization potential for a hole of the crystal. These changes in site energy can be separated into an intermolecular component and an intramolecular component. The intermolecular component is defined as the polarization energy and results from the interaction of the localized charge with the permanent and induce multipole moments of the surrounding crystal environment. The intramolecular component is the electron affinity or ionization potential of an isolated gas phase molecule. The site energy can be modulated by lattice vibrations and interaction with the surrounding environment. The coupling of the site energy with vibration modes is referred to as local (Holstein-type) electron-phonon coupling.

3.1.2 Electronic Coupling – Transfer Integral

The transfer integral, which represent the electronic coupling between adjacent molecules, is the dominant feature controlling charge transport in ordered organic semiconductor crystals and provides a measure of the delocalization of the carrier in the crystal.[29] The transfer integral, *J*, can be given by

$$J_{ij} = \langle \psi_i | H_{el} | \psi_j \rangle \tag{3.6}$$

where H_{el} is the effective one-electron Hamiltonian of the crystal and ψ_i and ψ_j are the HOMO and LUMO orbitals, of the isolated molecules, for hole and electron transport, respectively. Since the coupling is directional it plays a major role in the crystals charge carrier anisotropic nature. In a system with disorder, static or dynamic, the carrier states of the crystal could be treated as Bloch waves, similar to crystalline inorganic semiconductors, and the Bloch states would be calculated from the molecular orbitals of the isolated molecules.[74] With the introduction of disorder or fluctuations in the molecular positions the perfect periodic array of molecules would be disrupted and the changes in the magnitude of the transfer integral would occur. This change in transfer integral as a result of the change in the vertical (intermolecular separation) and horizontal (translation) displacement of the molecules can be seen in Figure 3.1

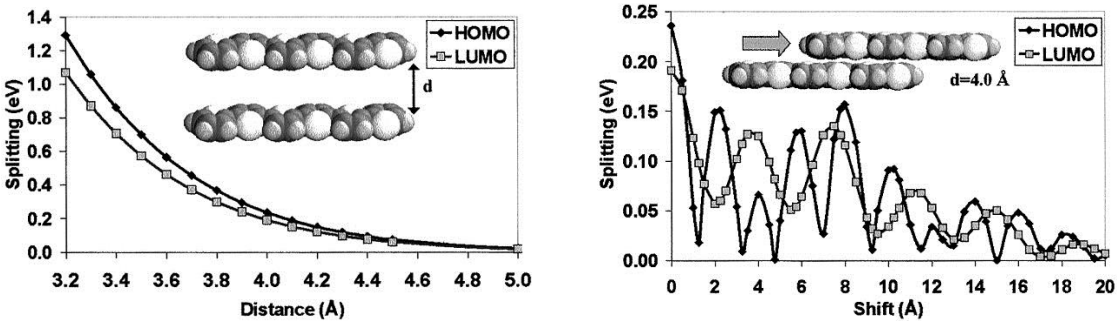

Figure 3.1: Left: Evolution of the INDO-calculated electronic splittings of the HOMO and LUMO levels in a cofacial dimer made of two sexithienyl molecules as a function of the intermolecular separation. Right: Evolution of the INDO-calculated electronic splittings of the HOMO and LUMO levels in a dimer formed by two sexithienyl molecules separated by 4.0 Å as a function of the degree of translation of one molecule along its main chain axis.[44] Reprinted with permission. Copyright 2002 National Academy of Sciences, U.S.A.

A common approach to calculating the transfer integral is the energy splitting in dimer (ESD) model. The ESD model uses two identical molecules in a cofacial arrangement and considers the splitting of the HOMO (LUMO) orbitals in the dimer with respect to an isolated molecule.[29] The transfer integral is calculated from the splitting of the HOMO (LUMO), $\Delta E = E_1 - E_2$, where:

$$J = \frac{\Delta E}{2} \tag{3.7}$$

This approach provides a good first approximation but is invalid for molecular orientations that are not cofacial or when the molecules are not equivalent.[44]

3.1.3 Electron Phonon Coupling

In a perfect world with no static or dynamic disorder, carriers would be freely delocalized and Bloch state band transport would dominate. But this ideal case is not possible due to intra-molecular and inter-molecular vibrations which tend to disrupt the delocalized carriers. These molecular vibrations can interact strongly with the charge carriers and these processes are referred to as electron-phonon coupling. Charge transport is affected by the motion of the atoms and molecules through the electron-phonon coupling modes, both local electron phonon and nonlocal electron phonon coupling.[29]

3.1.4 Local Electron-Phonon Coupling

Local electron-phonon coupling mechanism is defined from the Holstein model resulting from modulation by phonon modes of the site energies. The reorganizational energy, λ, associated with local electron-phonon coupling results from the charge transfer from one molecule to another molecule and is defined in the Marcus electron-transfer theory. The reorganizational energy has an intramolecular (internal), λ_i, and intermolecular (external) component, λ_e. The internal component represents a change of energy due to the modification of the equilibrium geometry of an individual molecule

going form a neutral state to an ionized state. The external component of the reorganizational energy results from the change in energy as a result of polarization and positions of molecules in the adjacent crystal lattice.[78] The external reorganizational energy for crystalline polyacenes is typically much less than that of the internal reorganizational energies with the external energies typically less than 10 meV and the internal reorganizational energies in the range of 100 – 200 meV.[79-80] Thus, external reorganizational energies are often neglected when considering the contribution of reorganizational energies on charge transport.

In the work by Holstein[64] it was shown that in the absence of electronic coupling between adjacent molecules (transfer intergral = 0) the charge would be localized on a single site by local electron-phonon coupling. The energy of the charge on that site that results from the change in molecular surroundings is stabilized by the polaron binding energy, E_p. The intramolecular reorganizational energy, λ_i, is calculated from the contributions from both molecules involved in the charge transfer. It takes in to account the relaxations energies of the molecule the charge is transferred to as well as from the molecule it is transferred from and is thus about twice the polaron binding energy (relaxation energy), $E_p = \lambda_i/2$.[80] This energy then plays a role in charge transport properties in the transport regime where the reorganizational energy is larger than the transfer integral.

3.1.5 Nonlocal Electron-Phonon Coupling

Nonlocal electron-phonon coupling arises from lattice phonons (inter-molecular vibrations) and the rotational and translational movement of molecules from their equilibrium sites in the crystal.[29, 69, 72] This intermolecular coupling is generally referred to as Peierls type[76] or Su-Schrieffer-Heeger type[81] interactions. At room temperature, the molecular movements are dominated by large low-frequency thermal motion. This movement is due to weak van der Waals interactions between molecules and the relatively large molecular masses common of materials found in crystalline organic semiconductors. These weak interaction and large masses result in weak restoring forces between the molecules and thus result in large amplitude and low frequency vibrational modes. These thermally activated intermolecular vibrations affect the orientation and distance of the wavefunctions between adjacent molecules and introduces modulation of the electronic coupling integral over time.[82]

3.1.6 Band Transport

Band transport is typically associated with inorganic semiconductors such as silicon and germanium.[55] Using a tight-binding model, when a number of interacting atoms are brought together, their energy levels split and become closely spaced forming

valence and conduction energy bands separated by a forbidden band gap. The coupling (transfer integral) between atoms can provide a measure of the width of the energy bands. Small coupling results in a narrow bandwidth with large effective carrier masses. Large coupling results in wider bandwidths and lighter effective carrier masses. Lighter carrier masses are easier to accelerate than heavier carrier masses. In crystals with long-range order and strong coupling between atoms the electronic states (charge carriers) become delocalized. These delocalized carriers can be thought of as delocalized wavepackets that are spread over a number of lattice sites. For band transport, the apparent mean-free-path, *l*, of the carrier is much greater than the lattice constant. In the case where the local electron-phonon coupling is negligible the delocalized wavepackets can be described semiclassically by the Boltzmann transport theory. The wavepackets can be scattered by phonons and impurities with the mobility of these carriers given by

$$\mu = \frac{et_s}{m^*} \tag{3.8}$$

where e is the elemental charge, t_s is the scattering rate and m^* is the effective mass.[54] The mobility decreases with increasing temperature as a result of an increased probability of phonon scattering. This dependence of mobility with temperature is taken to be a sign of band transport and follows a power law as

$$\mu \sim T^{-n}, \text{ where n = 1-3.}^{42} \quad (3.9)$$

3.2 The Role of the Polaron in the Development of Transport Theory

The observation of band-like behavior in organic semiconductors has led researchers to think about the transport in terms of traditional band transport where the carrier is highly delocalized with a large mean free path. But this analogy tends not to tell the entire story. A polaron based model where the carrier can be localized over a number of molecules and can be influenced by electron-phonon coupling has helped explain some of these experimental results.

As charges become localized on a molecular site due either to electron-phonon coupling or static disorder the charge can polarize the surrounding environment. This is especially relevant in conjugated materials where holes may be the dominant carrier type. The positive charge of the carrier will tend to polarize the electron rich π-orbitals in the conjugated systems effectively creating a polarized cloud around the charge creating a charge species referred to as a polaron.[83] Polarons can be classified as either small or large polarons depending on the electronic band width and the degree of electron phonon coupling. They can be viewed as being localized on a single molecular

site with a size smaller than the lattice constant (small polaron) or delocalized over several molecules with a size larger than the lattice constant (large polaron).[84]

3.2.1 Polaronic Band Transport

Large polarons result when the electronic coupling increases, as a result of wide electronic bands, and/or the electron-phonon coupling decreases. The wavefunction tends to become less localized and spreads over a number of lattice sites. At low temperatures, the carrier wavefunction is delocalized (wide bandwidth) and the polaron can be described as a large polaron with the associated lattice deformations spread out throughout the surrounding lattice.[67,85] The transport in crystalline organic semiconductors can be described using bandlike transport and the mobility is closely related to that given in Equation 3.9. As the temperature increases a decrease in the effective transfer integral occurs and the wavefunction is localized, the polaron band becomes smaller. An increase in temperature increases electron-phonon coupling increasing the carrier effective mass thus causes a reduction in the carrier mobility.[52, 86]

3.2.2 Small Polaron – Holstein Theory

Small polarons are a result of narrow electronic bands, low electronic coupling, and larger electron-phonon coupling. This leads to a localization of the wavefunction

on the molecular site with a size smaller than the lattice constant. Holstein[64-65] provide the initial work describing small polarons taking into account local electron-phonon coupling in carrier transport. This work focused on conditions where the local electron-phonon coupling was large with small electronic bandwidths localizing the charge. This scenario introduces a large energy barrier between neighboring sites restricting charge transfer. Charge transfer can occur by thermally assisted hopping or by a quantum mechanical tunneling process. For most conjugated materials, the Holstein model is applicable when the electronic coupling much smaller that the polaron binding energy (J << Ep). For the condition where J << λ and $\hbar w_0$ << k_BT the hopping rate can be given by

$$k_{hop} = \frac{J^2}{\hbar}\left(\frac{\pi}{k_B T \lambda}\right)^{\frac{1}{2}} e^{\frac{-\lambda}{4k_B T}}. \tag{3.10}$$

The carrier transport of a small polaron is thermal activated, and the mobility can be given by

$$\mu \sim L^2 k_{hop} \tag{3.11}$$

where L is the distance between hopping sites.[67]

3.3 Deviation from Traditional Models

The polaronic band model and the small polaron model provide the extremes of the delocalized and localized carrier regimes, respectfully. Ranging from the perfect Bloch-Boltzmann state type transport defining an ideal delocalized system with band like transport to a system with charge localization and transport occurring through a small polaron Marcus theory hopping transport model. In this picture, it can be reasoned that two main factors are then involved in the limits of carrier transport, the intermolecular coupling, J, and the relaxation energy, Ep. In the polaronic band model the intermolecular coupling, would then dominate and the relaxation energy, would be negligible. The opposite can then be stated for the small polaron model with the relaxation energy dominating and the intermolecular coupling being minimal. Neither of these limits are reached in high mobility organic semiconductors under normal operating conditions. This is due in part to the similar size of the energies of the transfer integral and the relaxation energy. Values for the transfer integrals are in the usually around, J ≈ 10 – 100 meV[48, 87] with relaxation energies around Ep ≈ 50 – 200meV.[88] This similarity in energies between the two competing models exempts either from playing a dominating role in the transport. Other factors that muddy the distinction of traditional transport models are the values of the intermolecular vibrational modes (≈ 10 meV)[89], intramolecular vibrational modes (≈ 100 – 200 meV)[48, 90-91] and the thermal energy at normal operating conditions (k_BT ≈ 25 meV). This overlap in energies

between the different contributing components makes it difficult to distinguish the underlying dominant feature controlling transport.

The validity of band transport can be questioned when one examines the apparent mean-free-path of the charge carrier in high purity organic semiconductor crystals. In Bloch-Boltzmann transport theory, the mean free path, l, of the carrier is much larger than the intermolecular spacing, a, with $l >> a$. Under this condition the wavefunction of the charge carrier is delocalized over a number of molecules. The Mott-Ioffe-Regel (MIR) limit ($l = a$) defines the lower bounds for the use of band theory in semiconductors.[92] With $l < a$, one would encounter short mean free paths suggestive of a localized carrier. The mean free path and the carrier mobility, to a first approximation, are proportional to the average time between scattering events, τ, where we can then infer: $l \sim \mu \sim \tau$. In materials with a large number of scattering events, this results in a shorter mean free path and lower mobilities. For band transport, where l is larger, we would expect a larger mobility. For band theory to hold, the experimentally determined mobility, μ, would then need to be higher than the mobility imposed by the MIR condition, μ_{MIR}, $\mu > \mu_{MIR}$. This is not the case with typical high mobility organic semiconductors. It has been shown, from band calculations, that for naphthalene, band transport is only valid for temperatures below 150 K and that the free path approaches 1 angstrom as T approaches 300 K (Figure 3.2).[51] Another example can be seen in the experimental results obtained from rubrene. The highest room temperature FET mobility values are generally in the range of 10 – 20 $cm^2V^{-1}s^{-1}$. Calculated mobility measurements imposing the MIR condition gives a mobility of 23 $cm^2V^{-1}s^{-1}$.[71] These

results thus put some doubt on the treatment of band transport for organic semiconductor materials.

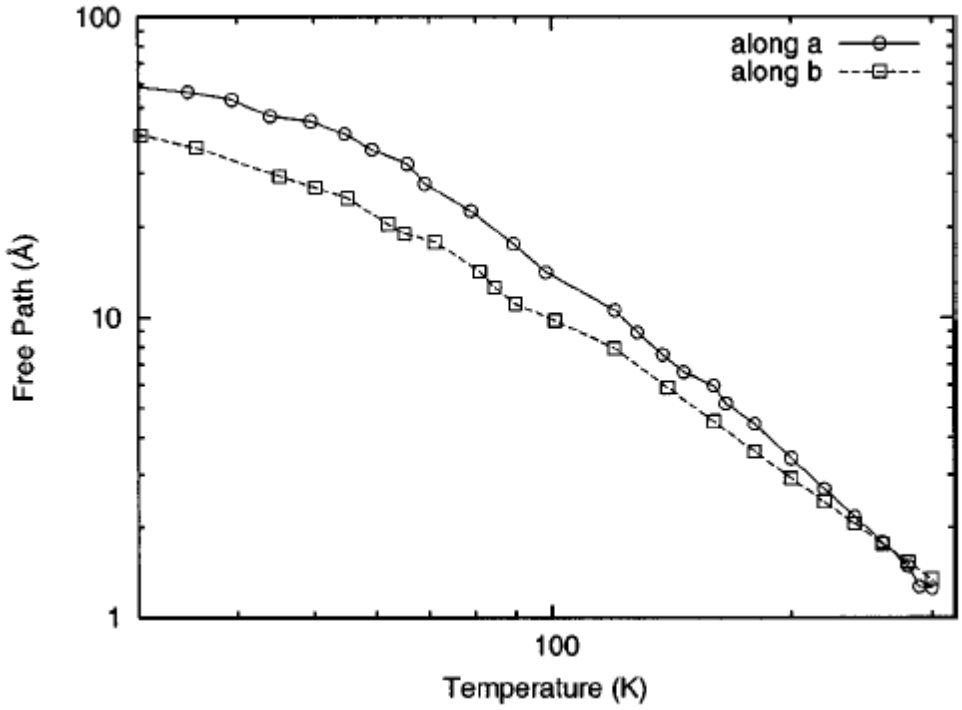

Figure 3.2: Temperature dependence of calculated hole mean free path for a naphthalene crystal along crystal **a** and **b** directions.[51] Reprinted with permission. Copyright 2003 AIP Publishing.

On the other extreme is small polaron transport, where the carrier is localized on a molecular site and transport occurs by thermally assisted hopping, also does not describe charge transport in organic semiconductors. In this case the relaxation energy, Ep, would be the dominate energy of the system, larger than the intermolecular coupling term, J, where Ep > J. This would localize the carrier on a molecular site. There are two facts that can be argued against the small polaron model. First, the calculated

relaxation energies are too small for small polarons to form and be stable. The relaxation energy measures the strength of the interaction of the charge carrier and intramolecular phonons. This energy is related to the electronic and geometric structure of the molecule and the other dynamic factors that affect transport. Is has been shown that the calculated relaxation energies decrease with increasing number of atoms in the conjugated molecule. Theoretical relaxation energies of 68 meV, 56 meV and 48 meV for anthracene, tetracene and pentacene have been reported.[88] Figure 3.3 shows this inverse relationship for hole and electron-vibrational coupling. Larger molecules such as rubrene would then be expected to exhibit small relaxation energies. With relaxation energies on the order of the intermolecular coupling energies there is a lower probability of small polaron formation. It would be expected that intermolecular vibrations would tend to disrupt small polaron formation at these levels of relaxation energies. A second feature that would tend to discredit small polaron creation is the fact that most organic semiconductors exhibit bandlike mobilities. In bandlike transport the mobility increases with decreasing temperature. This contradicts the underlying premise of thermally activated hopping transport, increasing mobility with increasing temperature, associated with Marcus theory and Holstein small polarons.

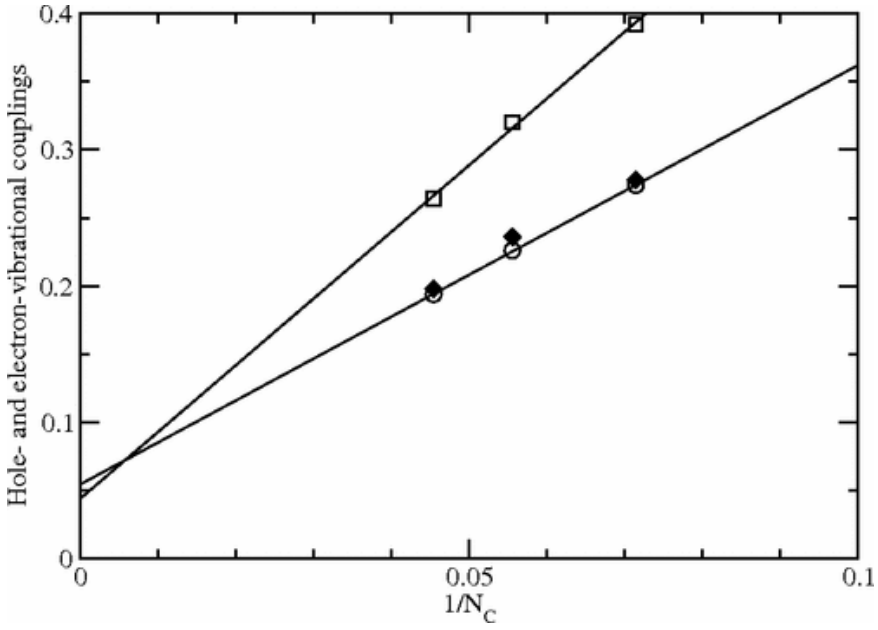

Figure 3.3: Hole-vibrational coupling [◆-Experimental, ○-Theoretical] and electron-vibrational coupling [□-Theoretical] vs the inverse of the number of carbon atoms in anthracene, tetracene, and pentacene.[88] Reprinted with permission. Copyright 2002 American Physical Society.

3.3.1 Transient Localization: Nonlocal Electron-Phonon Coupling Revisited

Since neither band or small polaron hopping transport provide a comprehensive picture of the charge carrier dynamics of crystalline organic semiconductors at ambient operating conditions, an alternative approach to understanding the transport mechanism is needed. Carrier coupling to low-frequency intermolecular vibrations has come to the forefront in this discussion. This type of interaction has been discussed previously[93-94]

and has recently been revisited as playing a dominant role to explain experimental transport results.[67, 74, 95-98] As described earlier, the large molecular motions are due to the weak van der Waals forces that are present between molecules in these crystal systems. The weak restoring forces result in large amplitude low-frequency modes. The molecular displacements create fluctuations in the transfer integrals over time and the charge dynamics then fluctuate between areas of high overlap and charge delocalization and areas of low overlap and charge localization. These fluctuations in the transfer integral with molecular displacement can be seen in Figure 3.1, which illustrates the electronic splitting of the HOMO/LUMO which can be related to the fluctuations of the transfer integrals. This dynamic disorder results in what has been termed transient localization where the carrier is 'momentarily' localized on a molecule before reaching a stage where delocalization and transport can occur.

A simple Hamiltonian, using a tight-binding approximation, can be written to describe the low frequency modes along a 1D chain[71]

$$H = -J\sum_{i}[1-\alpha(\mu_i-\mu_{i+1})](c_i^{+}\,c_{i+1}+c_{i+1}^{+}c_i)+H_{vib} \qquad (3.12)$$

where

$$H_{vib} = \sum_{i}\frac{M\omega_0^2}{2}u_i^2+\sum_{i}\frac{p_i^2}{2M}. \qquad (3.13)$$

The coordinates for the translational or rotational displacement of the individual molecules are given by $\mu_i-\mu_{i+1}$, Figure 3.4. It is this displacement that modulates the

amplitude of the transfer integral, J, as $J_{i,i+1} = J\,[1 - \alpha(\mu_i - \mu_{i+1})]$ where α is the electron-phonon coupling constant. The hopping between orbitals on neighboring molecules is given by the creation (annihilation) operators, $c_i^+(c_i)$. The vibrational term, H_{vib}, represents the movement of the molecules around their equilibrium positions. Typical molecular semiconductors have relatively big masses and with weak restoring forces, this results in small intermolecular vibrational frequencies of $\hbar\omega_0 \leq 10$ meV.

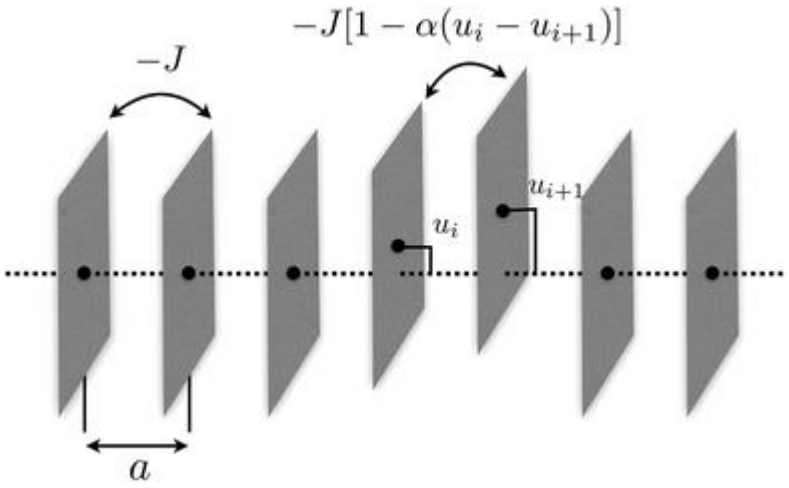

Figure 3.4: 1D molecular chain showing modulation of transfer integral, J, by molecular displacement, $\mu_i - \mu_{i+1}$. a is the lattice parameter. α is electron-phonon coupling constant.[71-72] Reprinted with permission. Copyright 2006 American Physical Society.

In this picture, where the transport is a function of the intermolecular coupling and small polaron formation, and where each is perturbed by the large amplitude low-frequency modes, the mobility can be characterized by how far the charge can delocalize in a given time period and how long it is localized on a molecular site. These dynamics

can be defined as the transient localization length, l_{loc}, and the propagation rate, ω. The time a charge is localized on a molecular site can be represented as ω^{-1} and the localization length, l_{loc}, the distance the charge can delocalize in that time period. The mobility can then be calculated using

$$\mu = \frac{e}{k_B T} \, l_{loc}^2 \omega. \tag{3.14}$$

As temperature decreases, dynamic disorder decreases (intermolecular coupling increases) which would allow l_{loc} to increase resulting in a larger mobility. This relationship could explain the band-like transport observed in crystalline organic semiconductors.

3.3.2 Transport in Rubrene – ab plane – Transient Localization

The highest carrier mobilities in rubrene occur within the **ab** plane with calculated electronic couplings of 21 and 140 meV in the **a** and **b** directions, respectively.[73] Transport in the **ab** plane of rubrene exhibits bandlike temperature dependence but does not fulfill band transport due to the fact that the localization length is shorter than the unit cell. There is still a need to validate the concepts of transient

localization as applied to crystalline organic semiconductors. Recent results investigating this idea in rubrene crystals demonstrate the potential of this treatment.

The modulation of the intermolecular transfer integral for a rubrene crystal at different temperatures was calculated by molecular dynamic simulations and quantum chemistry computational methods.[99] The probability distribution of the transfer integral between HOMOs for two different electronic coupling directions were calculated for three different temperatures is shown in Figure 3.5. The results indicate the distributions for the two separate transfer integrals for the A and B direction are gaussian in nature and widen with increasing temperature. This increase in energy distribution with increasing temperature helps confirm the dynamic disorder model.

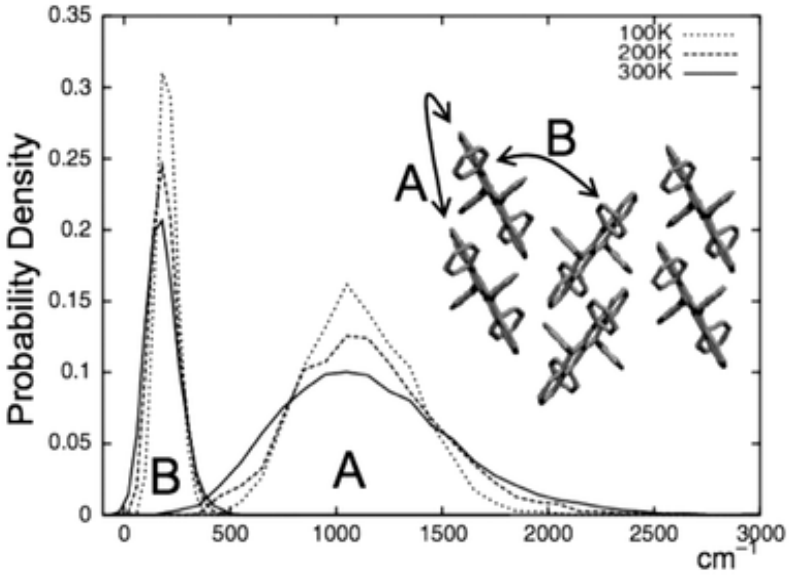

Figure 3.5: Probability density distribution as a function of energy of the transfer integrals in two directions, A and B, in rubrene crystal.[99] Reprinted with permission. Copyright 2007 John Wiley & Sons, Inc.

Experimental evidence for transient localization was recently demonstrated using ^{13}C-rubrene in a FET configuration.[95] The substitution of the ^{13}C isotope in rubrene would increase the molecular mass which would decrease the intermolecular vibrational frequency. The decrease in vibrational frequency would tend to increase the time the carrier stays localized thus decreasing the mobility as per Equation 3.14. These results showed a 13% decrease in the mobility for the ^{13}C rubrene compared to unsubstituted rubrene. The authors reported single crystal rubrene FET mobilities at room temperature of 12.6 ± 0.7 $cm^2 V^{-1}s^{-1}$ for ^{13}C-rubrene and 14.6 ± 0.7 $cm^2 V^{-1}s^{-1}$ for unsubstituted rubrene. This provides solid evidence for the dynamic disorder model as applied to the **ab** plane in rubrene.

3.3.3 Transport in Rubrene – c direction – Incoherent Hopping

Transport in the **c**-axis direction in crystalline rubrene has been reported to be around 0.3 $cm^2V^{-1}s^{-1}$, two orders of magnitude lower than in the **ab**-plane. The calculated electronic coupling in the **c**-direction has been reported to be around -2.7 meV.[73] The transport between the **ab** plane and **c**-direction is not coupled, with the transport in the **ab**-plane occurring at a greater rate than the transport in the **c**-direction. It has been proposed that the transport in the **c**-direction in rubrene occurs by incoherent hopping between a delocalized wavefunction on a **ab**-layer to an adjacent **ab**-layer.[73] The mobility observed by these hopping events can be derived from Fermi's golden rule

and is given in Equation 3.14. This incoherent hopping between **ab** planes can be seen in Figure 3.6.

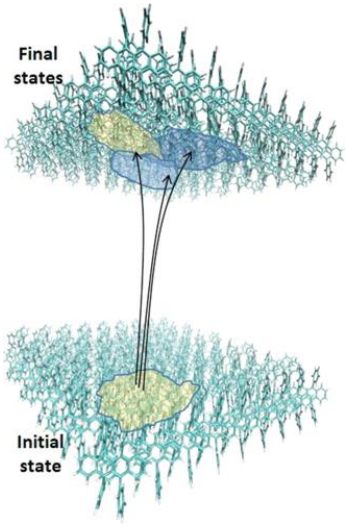

Figure 3.6: Charge hopping in the c-direction of rubrene.[73] Reprinted with permission. Copyright 2016 American Physical Society.

Chapter 4

Methods for Determining Single Crystal Carrier Mobilities

A number of experimental techniques have been used to measure carrier mobilities. These techniques include time-of-flight (TOF), field effect transistors (FET) and surface acoustic wave (SAW). Other methods such as xerographic discharge, Hall Effect, and cyclotron resonance have also been used but these tend to provide less reliable data. A number of authors provide a more detailed discussion of these techniques.[25, 66, 100-102] This chapter will review the TOF technique to examine vertical (bulk) and lateral (surface) carrier mobilities. Although TOF is the measurement technique used in this study to examine charge carrier mobilities, a discussion of the field effect transistor technique will be given to allow a comparison with the Lateral Field (surface) TOF measurements.

4.1 Time-of-Flight (TOF) – General Considerations

TOF is used to measure the transient response of the drift of photoinjected carriers in both crystalline and amorphous materials and is useful for materials that

display high resistivity and low carrier mobilities. Time-of-flight (TOF) was first demonstrated as a technique for determining the carrier mobility in selenium by Spear,[103-104] Kepler[105] and LeBlanc[106] then applied it to organic semiconductor materials to investigate electron and hole mobilities in anthracene crystals. Karl *et al.*, performed seminal TOF experiments examining the low temperature and anisotropic mobilities in organic single crystals.[107-109]

4.1.1 Vertical (Bulk) TOF

In vertical (bulk) TOF, carrier mobility is measured through the thickness of the material. The crystal or thin film of thickness *L* is placed between two electrodes with one of the electrodes being transparent to an applied excitation source. A voltage source, *V*, is attached to the sample across the electrodes with the polarity of the voltage source determined by the carrier to be measured, electron or hole. The measuring circuit is completed by the addition of a load resistor, *R*, attached to an oscilloscope to measure the resulting current pulse. Electron-hole pairs are photo-excited near the surface of the material by a short pulse of radiation, typically a laser pulse, and transported through the sample by the applied electric field. The current created by the transported charge carrier is determined by measuring the voltage drop across an external resistor using an oscilloscope. A typical TOF experimental setup is shown in Figure 4.1.

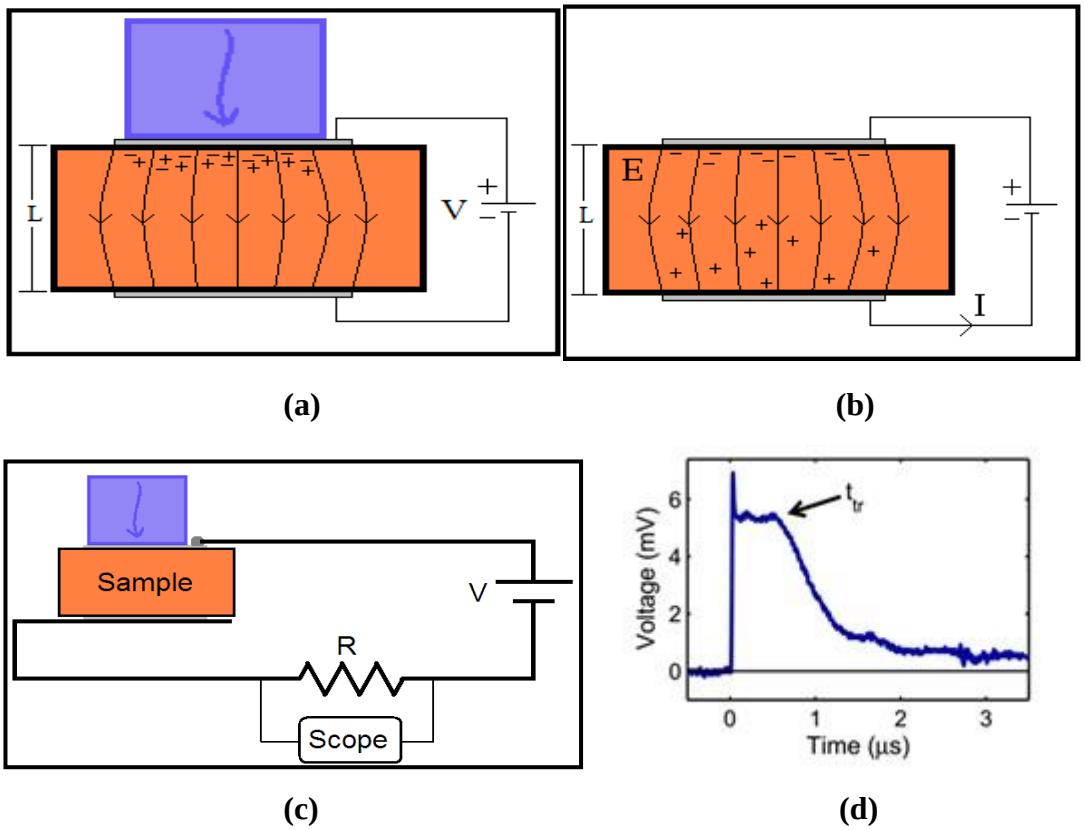

Figure 4.1: Typical TOF sample geometry. a) Initial conditions with applied voltage, V and laser pulse shown in blue creating charge carriers. b) Intermediate conditions after laser pulse showing carriers drifting through the sample to the opposite electrode. c) Complete circuit. Current (I) is measured as a voltage drop across resistor, R. L = sample thickness. E = electric field. d) TOF voltage pulse showing transit time, t_{tr}.[35] Reprinted with permission. Copyright 2015 AIP Publishing.

A typical transient current pulse is shown in Figure 4.1d. The charge carrier mobility is calculated from the transit time, t_{tr}, of the current pulse (the time it takes the carriers to reach the collecting electrode). The mobility of the charge carrier is given by

$$\mu = \frac{L^2}{t_{tr}V} \tag{4.1}$$

where L is the thickness of the sample and V is the applied potential across the sample.

Since the charge carriers are created in the sample and not injected into the sample through an electrode, TOF mobility measurements are not influenced by electrode preparation and charge injection effects. The anisotropic nature of the crystal can also be examined using TOF. The direction of the applied bias can be oriented in any crystallographic orientation. Also, since either a negative or positive bias can be applied across the sample, both electron and hole carrier mobilities can be measured on the same sample. One limitation is that the sample must be photoconductive, which is generally the case with organic materials. If the material is not photoconductive a photo-injecting electrode may be used.[110]

There are several factors in the experimental design that must be met to ensure a proper measurement. The absorption depth, δ, of the laser pulse in the material should be much less than the thickness, L, of the sample. A shallow absorption depth will allow for the carrier that is not transported across the sample to be quickly collected on the top electrode thus minimizing any effect on the internal electric field. The excitation laser pulse width, t_x, should be much less than the transit time, t_{tr}, the time it takes the carriers to cross the sample.[111-112] A short excitation time will also create a carrier packet with a narrow width, w, much less than the sample thickness. One must also ensure that the number of charge carriers produced, N, by the excitation source be such that the space charge created in the sample by the charge separation is small as to not affect the

externally applied electric field. The effects of these experimental limitations can be seen by examining the internal electric field in the presence of the drifting sheet of charge carriers as shown in Figure 4.2.

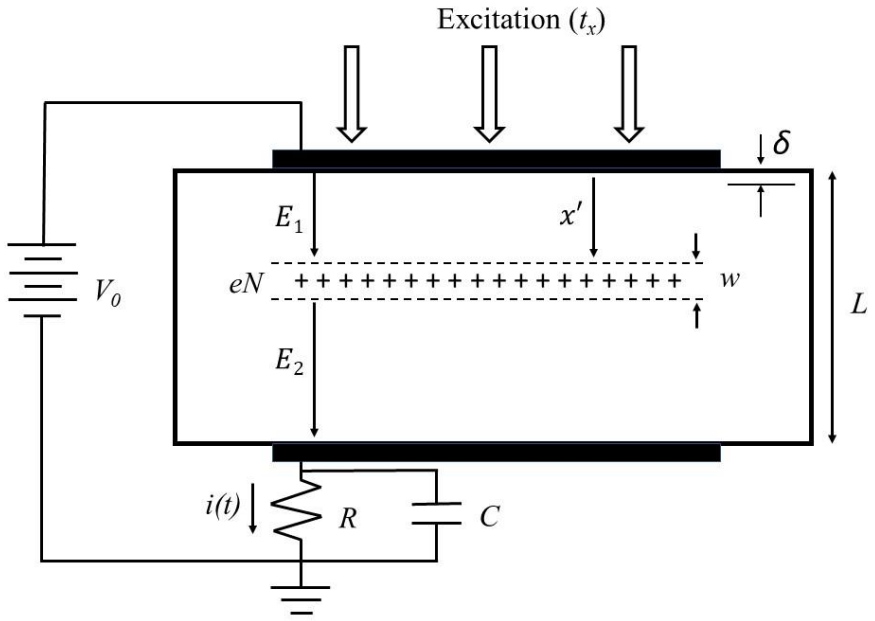

Figure 4.2: Electric fields in a highly resistive sample in the presence of a drifting sheet of charge carriers.

$$E_1(x') = E_0 - \frac{eN}{\varepsilon}\left(1 - \frac{x'}{L}\right) \tag{4.2}$$

$$E_2(x') = E_0 + \frac{eNx'}{\varepsilon L} \tag{4.3}$$

where $E_0 = V_0/L$ is the applied electric field, ε is the dielectric permittivity of the sample and N is the concentration of charge carriers, holes in this example. From these

equations, it can be seen that the internal electric field can be affected by the drifting charge carriers. If the number of charge carriers, N, is kept small so the field induced by the carriers is much less than the applied field, $eN/\varepsilon << E_0$, the internal electric field can be considered constant throughout the sample and equal to V_0/L.

The photocurrent can be used to measure the drift mobility of the carriers when the created charge, Q_0, is much less than the charge on the electrodes, V_0C, where C is the sample capacitance which includes the sample, leads and scope input capacitance. The condition where $Q_0 << V_0C$ satisfies the small signal condition and leads to a uniform internal electric field where $E_0 = E_1 = E_2 = V_0/L$ and the carrier packet drift velocity can be assumed to be constant. The analysis of the TOF signal becomes more complicated when the small signal condition is not met and the space charge effect caused by excess carriers must be considered.

The RC time constant of the experimental setup can also affect the transient current and must be considered. The RC time constant is calculated from the external resistor and the capacitance of the sample.[113] There are two methods for determine the transit time in TOF measurements. They are identified by the magnitude of the RC time constant of the circuit in relation to the transit time. They can be defined as: 1) the charge integration method where $RC >> t_{tr}$ and 2) the current pulse method where $RC << t_{tr}$.[111]

In the integration method, the charge is integrated over time due to the rise time of the circuit being much longer as compared to the transit time. The charge on the contacts are re-distributed due to the changing internal fields of E_1 and E_2. The changing charge on the bottom contact can be given from the change in E_2 as

$$\Delta q(t) = \frac{Nex'}{L} \tag{4.4}$$

From $\Delta q(t) = C\Delta V(t)$, this results in a changing potential across R for $0 < t < t_{tr}$ given by

$$\Delta V(t) = \frac{Ne}{CL} v_d t \tag{4.5}$$

where v_d is the drift velocity, $v_d = L/t_{tr}$. For times larger than the transit time, $t \geq t_{tr}$, $\Delta V = Ne/C$ and remains constant. This linear increase in q up to t_{tr} with a plateau in q after t_{tr} can be seen in Figure 4.3a. Figure 4.3a represents an ideal case with no carrier trapping.

In the current pulse method, the size of R is decreased and the rise time of the circuit is rapid due to the much smaller RC time constant. Using the relations $q = it$ and $v = x/t$, Equation 4.4 becomes

$$i = \frac{Nev_d}{L} \tag{4.6}$$

and for $0 < t < t_{tr}$, the voltage drop across R becomes

$$\Delta V = R\frac{Ne}{L}v_d \tag{4.7}$$

For times large than the transit time, $t \geq t_{tr}$, $\Delta V = 0$. The current pulse, which for a nontrapping situation, resembles a square wave, is shown in Figure 4.3b.

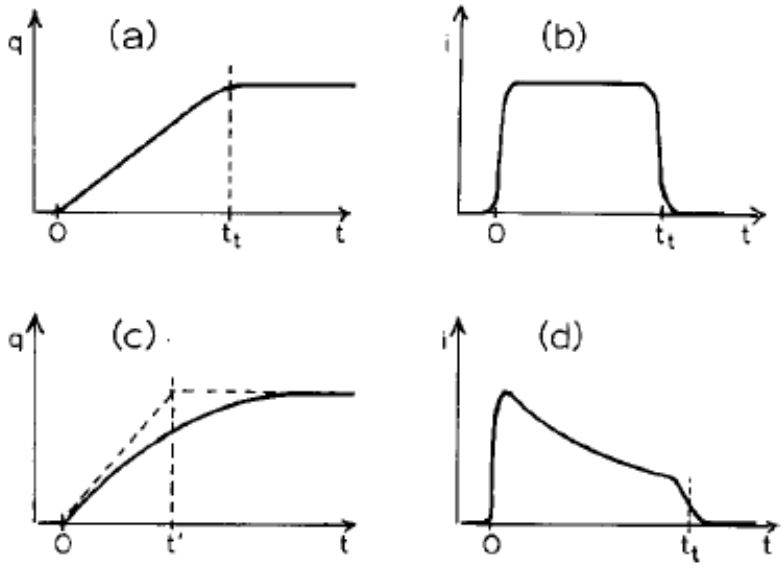

Figure 4.3: Typical pulse shapes observed in drift mobility experiments when the carriers are generated close to the top electrode, $\delta << L$, (a) integrated signal $CR >> t_{tr}$ (b) current pulse, $CR << t_{tr}$. In both (a) and (b) deep trapping is absent. (c) and (d) show corresponding pulse shapes when the drifting carriers interact with deep centers.[111] Reprinted with permission. Copyright 1969 Elsevier.

The shape of an ideal initial charge packet at time = 0, can be viewed as a delta function, δ(t=0). The spreading of the pulse can be modeled as a Gaussian-type

broadening as a result of trap and release times of the carriers.[114] The shape of the current pulse can provide information on the trap sites in the material. Shallow traps are those with trap release times that are much less than the transit time and deep traps are those with trap release times greater than the transit time. Figure 4.4 shows a representation of the trap depths relative to HOMO and LUMO bands in a rubrene single crystal OFET.

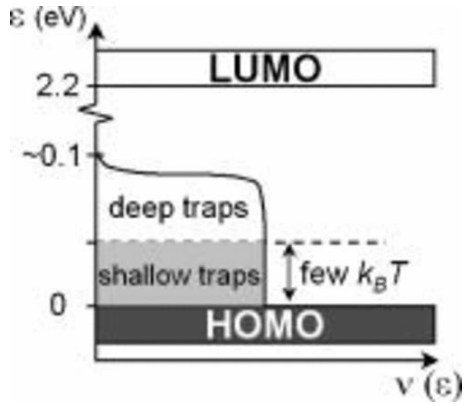

Figure 4.4: Schematic diagram of the energy distribution of localized electronic states in the energy gap between HOMO and LUMO bands in rubrene single-crystal OFETs.[59] Reprinted with permission. Copyright 2006 American Physical Society.

While both types of traps have an influence on transit time, shallow traps tend to decrease the carrier mobility (increase the transit time) due to the trap and release process by broadening of the charge packet. In shallow trapping charge carriers are typically trapped and subsequently thermally released on a time scale less than the overall transit time. The effective transit time, as a result of shallow trapping, is the sum of the transit time with no trapping and the average trap time

$$t_{eff} = t_0 + Nt_{tp} \quad (4.8)$$

where t_{eff} is the effective transit time, t_0 is the trap free transit time, N is the number of trap incidents and t_{tp} is the average trap time.[115] The mobility of the carrier can then be calculated from Equation 4.1 using t_{eff}. In situations where the trap times are much less than the mean transit time the carrier packet reaches equilibrium and the drift velocity of the packet is constant. This type of carrier transport is generally referred to as nondispersive transport and is consistent with a rectangular shaped current pulse, Figure 4.3b.[116]

Deeper trapping on the other hand, can result in carriers being held for times longer than the transit time. These deeper trap centers may or may not release the carriers during the time frame of the experiment. Deep trap carriers with time frames slightly longer than the transit time (those released during the experiment) can be gradually released. These released carriers cross the crystal with transit times longer than the average transit time resulting in tailing of the current pulse (Figure 4.3d). This is a result of a nonequilibrium condition being establish for the movement of the carrier packet due to longer hopping times of the carriers. This type of transport is referred to as dispersive transport and can be described by the Continuous-Time-Random-Walk model.[112]

These models are applicable for simple systems where there may be a single trap state with a constant depth. As the system becomes more complex, such as multiple trap states with varying trap depths, these models must be expanded. Other issues such

as non-ideal charge carrier generation, space charge effects, carrier concentration gradients, inhomogeneous applied fields, nonuniform sample thickness and carrier diffusion processes can lead to variations in the shape of the current pulse.

The density and the energy of shallow trap states can be determined from the measurement of carrier mobilities. The relationship between the trapping lifetimes, the density of states of the conduction bands and trap bands and the effective mobilities was first derived by Schockley and Read.[117] At low temperatures, this relationship becomes simply

$$\mu_{eff} = \mu_0 \frac{N_c}{N_t} \exp(-\frac{E_t}{kT}) \tag{4.9}$$

where μ_{eff} is the effective mobility, μ_0 is the trap free mobility, N_c is the density of states in the conduction band, N_t is the density of trap states and E_t is the energy of the trap state.[114] A plot of μ vs 1/T will yield the activation energy of the trap site.

4.1.2 Lateral (Surface) TOF

The applications of organic molecular semiconductors as active elements in photovoltaics and field effect transistors depend on efficient charge transport. These

devices share a property, namely that the charge transport occurs primarily on or near the surface of the semiconductor material. The applications of organic molecular semiconductors as active elements in photovoltaics and field effect transistors (FETs) depend on efficient charge transport on and within a few molecular layers of the surface.[118] Studying surface charge carrier mobility of organic semiconducting materials is important in technological advancements for faster, cheaper, lighter, and more flexible organic electronics. Nano-scale structure and charge transport characteristics are often very different at the surface, as opposed to the bulk of a material. The manner by which charge carriers actually travel across the surface is not completely understood. Factors that have been known to affect the rate carriers travel include molecular packing, structural defects, potential energy trap sites including surface oxidation sites.

Lateral field-time of flight (LFTOF) provides an avenue for probing carrier mobility at or near a materials surface. The LFTOF method has the potential to study surface charge carrier mobility, in a similar manner as the FET method, while avoiding charge injection effects and gate composition-dependent measurements commonly associated with the FET technique. LFTOF has seen limited use but has been demonstrated on single crystalline diamond films[119-120] organic films,[121-122] and recently on perylene single crystals[123].

LFTOF is a technique resulting from the charge carrier separation by means of a photoinduced laser pulse on the materials surface. Electron-hole pairs are photo-

excited on the semiconductor surface. The generated charge carriers travel across the material by means of an applied external field towards a collection electrode for measurement as shown in Figure 4.5. The carriers are moved from the photogeneration point to the opposite electrode through a distance by an applied voltage. The carriers create a current pulse which is characterized by a transit time and the charge carrier mobility can then be calculated as in bulk TOF. This provides an intrinsic measure of the transport properties on or near the surface of the material. By measuring the resulting current, the transport, recombination and trapping of charge carriers can also be studied.[119]

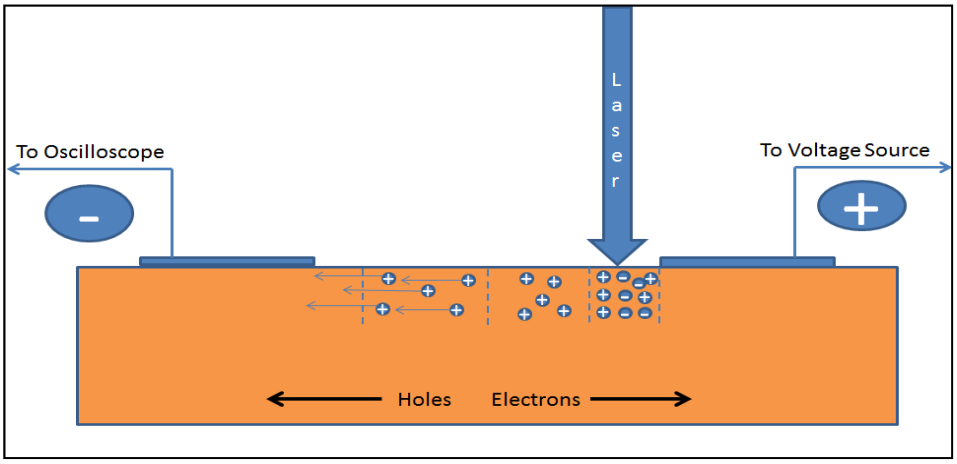

Figure 4.5: LFTOF charge carrier creation and transport.

4.2 Organic Field Effect Transistor (OFET)

The organic field-effect transistor has become a widely used technique for the electrical characterization, including carrier mobility, of organic semiconductor materials. It is also useful in realizing the potential of these materials for applications in integrated circuits and a wide range of electrooptic devices.

The structure of an OFET consists of source, drain and gate electrodes along with an active layer comprised of the organic semiconductor and a dielectric material between the active layer and the gate electrode. A number of device structures are possible for the orientation of the electrodes and active and dielectric layers depending on the materials used and processing conditions as shown in Figure 4.6.

The movement of the carriers through an OFET is controlled by a voltage applied to the gate electrode, which affects the dielectric material, and the bias between the source and drain. Charge carrier transport takes place in the organic semiconductor from the source to the drain. The current path between these two terminals is called the channel. Organic semiconductors are effectively electrical insulators so for a current to flow, carriers are supplied by injection into the organic semiconductor from the source electrode. The semiconductor layer may be made of either a p-type or an n-type semiconductor material. The gate dielectric materials can be either an inorganic material such as SiO_2, an insulating organic polymer or air.

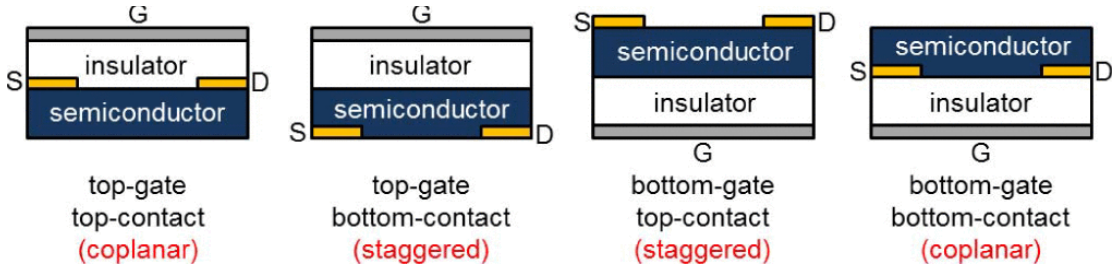

Figure 4.6: Different OFET geometries determined by the order of stacks and relative positions of contact electrodes. G: gate. S: source. D: drain.[124] Reprinted with permission. Copyright 2014 IEEE.

Following a more detailed analysis, the operation of the OFET is controlled by the application of a voltage to the gate electrode (V_g) and to the drain electrode (V_d) with the source electrode usually held at ground ($V_s = 0$). When a voltage is applied to the gate, the gate voltage will create a channel of charges of opposite polarity than V_g along the dielectric/organic semiconductor interface as seen in Figure 4.7b. For a material where the major carrier is the hole, a p-type OFET, a negative voltage is applied to the gate and holes in the organic semiconductor layer accumulate at the dielectric interface. The width of the channel and the number of carriers at the interface is dependent on the capacitance of the dielectric, C, and V_g. The magnitude of the current through the device is controlled by the applied gate voltage. The OFET is considered to be in the off-state when no voltage is applied to the gate although there may be a small leakage current flowing between the source and drain. The application of a voltage between the drain

and source, V_{ds}, will then produce a current between the source and drain, which for a p-type material consist of a hole carrier. Due to disorder at the semiconductor/dielectric interface trap states will be present at the interface. Charges that accumulate at the interface will fill these deep trap states will not be mobile. An additional gate voltage to is needed to create free carriers. This additional voltage is referred to as the threshold voltage, V_{th}, resulting in an effective gate voltage, V_g - V_{th}.

When a small V_{ds} is applied, where $V_{ds} << V_g$ - V_{th}, the current flowing through the channel, I_d, is linear in respect to V_{ds} as shown in Figure 4.7b and is referred to as the linear region. As V_{ds} is increased to the effective gate voltage, V_g - V_{th}, free carriers are depleted in the area near the drain. This is a result of an increase voltage near the drain, $V(x)$, and that the difference between V_g and $V(x)$ is less than V_{th} so no free carriers can accumulate resulting in the channel being pinched off as seen in Figure 4.7c. Due to the high field that develops between the pinch-off point and the drain, a saturation current, I_{sat}, can flow from the remaining channel to the drain. As V_{ds} increases the channel shortens as the depletion region increases but the current, I_d, does not appreciable increase. This can be seen in Figure 4.7d and is referred to as the saturation region. The on/off current ratio of the device is the ratio of the saturation current to the leakage current.

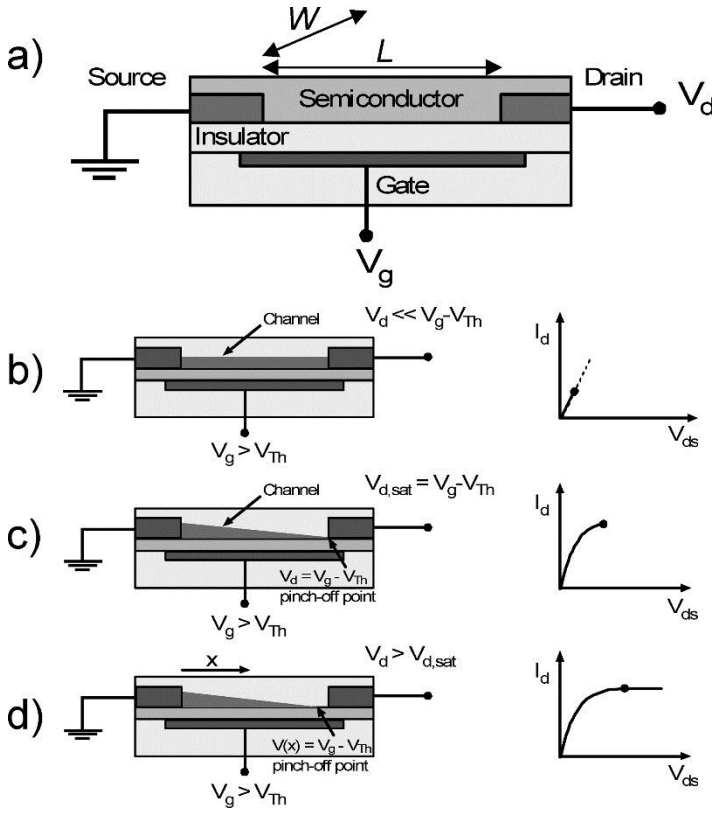

Figure 4.7: (a) Schematic structure of a field-effect transistor and applied voltages**:** L = channel length; W = channel width; V_d = drain voltage; V_g = gate voltage; V_{Th} = threshold voltage; Id = drain current. (b−d) Illustrations of operating regimes of field-effect transistors: (b) linear regime; (c) start of saturation regime at pinch-off; (d) saturation regime and corresponding current−voltage characteristics.[125] Reprinted with permission. Copyright 2007 American Chemical Society.

The current flowing through the channel can be controlled by the gate voltage and the source-drain voltage. For a given gate voltage, the current through the channel from the source to drain electrode is linear with an increasing applied source-drain voltage and slowly saturates as shown in Figure 4.8. The relationship between these variables is what defines the performance of the device. The main device characteristics derived from the operation of an OFET are the charge carrier mobility, the on/off current

ratio and the threshold voltage. Device characterization utilizes two different sets of measurements. One set of measurements is referred to as the output curves and is obtained from varying the gate voltage and measuring the source-drain current at different source-drain voltages as shown for rubrene single crystals in the lower panel in Figure 4.8. The second set of measurements, shown in the top panel of Figure 4.8 consists of measuring source-drain current at different gate voltages and is referred to as the transfer curve.

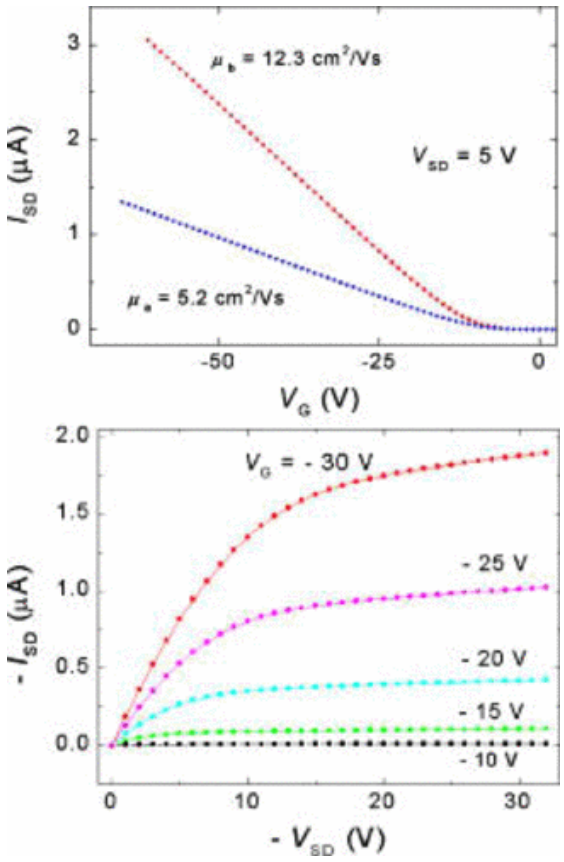

Figure 4.8: Characteristics of rubrene single-crystal OFETs**:** transconductance/transfer curves, $I_{SD}(V_G)$ (upper panel) and output curves, $I_{SD}(V_{SD})$ (lower panel). Upper panel also shows mobility in the **a** and **b** crystal directions.[59] Reprinted with permission. Copyright 2006 American Physical Society.

The current and carrier mobility for OFETs can be calculated from the applied voltages and the device parameters using relationships of the drain current derived from the traditional inorganic MOSFET model.[2] The current in the linear range is given by

$$I_{SD}^{lin} = \mu_{lin} \frac{W}{L} C(V_G - V_{th})V_{SD} \tag{4.10}$$

and in the saturated range is given by

$$I_{SD}^{sat} = \mu_{sat} \frac{W}{2L} C(V_G - V_{th})^2 \tag{4.11}$$

The carrier field-effect mobility can be calculated from the slope of the linear region, the transconductance, which is defined as the change of I_{SD} with V_G at a small V_{SD}, of the transfer curve and by solving, I_{SD}^{lin} for μ_{lin} :

$$\mu_{lin} = \left(\frac{L}{WCV_{SD}}\right)\left(\frac{\partial I_{SD}}{\partial V_G}\right) \tag{4.12}$$

The mobility in the saturated region can be derived from the slope of the square root of I_{SD}^{sat} as a function of the gate voltage:

$$\mu_{sat} = \left(\frac{2L}{WC}\right)\left(\frac{\partial \sqrt{I_{SD}}}{\partial V_G}\right)^2 \tag{4.13}$$

4.3 TOF vs FET

The techniques used to measure carrier mobilities can mask the intrinsic electronic properties of the material. As can be seen from this brief discussion of OFETs, there are a number of variables involved that can affect the determination of the carrier mobility using the FET technique. To get a clearer understanding of the intrinsic mobility due to just the chemical structure and solid-state packing of the molecules one needs to eliminate any extrinsic factors that may cloud the true parameters controlling charge transport. With this said, determining the intrinsic factors is just part of the overall effort to implement these materials in useful devices. Issues such as contact injection barriers and dielectric effects need to be understood to optimize device performance. There is also an issue with the potential differences in device characteristics reported from different research labs due to different methods of device fabrication and characterization. There is an effort to standardizing fabrication and characterization OFETs to provide a measure of consistence between different groups.[126]

Some issues that may arise when interpreting mobilities determined using field effect techniques include:

- The potential for high carrier density in the FET device. When carrier density becomes very high the distance between carriers may approach the size of a small polaron in the material resulting in interactions between the carriers.

- The polarization of the gate dielectric may affect the motion of the carrier in the conduction channel.

- Surface states on the crystal may affect mobilities due to different surface packing than in the bulk and the possibility of oxidized or contaminated surface states.

- In OFET measurements, charges are injected into the device. This leads to concerns of contact effects and injection barriers at the contact interface.

The use of Time-of-Flight (TOF) photoconductivity techniques to measure mobilities can circumvent these issues and provide a clearer picture of the intrinsic mechanisms involved in carrier transport. Advantages of using TOF to determine carrier mobilities include:

- There are no injection or contact effects since the carriers are photogenerated in the material and not injected.

- The charge density can be controlled by regulating the excitation flux, which allows the carrier density to be kept at a level where the interaction between polarons is not a factor.

- Both electron and hole mobilities can be independently measured on the same sample by changing the polarity of the applied electric field.

Taking these issues into consideration, Lateral-Field TOF, with its inherent advantages over field effect techniques, may be a useful technique to measure the

intrinsic mobility on the surface of the crystal for comparison with field effect mobility measurements.

Chapter 5

Experimental Methods and Instrumentation

This chapter deals with crystal growth, crystal selection and crystal sample preparation as well as instrumentation design for the vertical and lateral TOF. Experimental results for vertical TOF and lateral TOF measurements are given in Chapter 6.

5.1 Growth and Characterization of Single Crystals

5.1.1 Crystal Growth-Physical Vapor Transport

Growth of single crystals with high purity, long range order and with dimensions large enough to be characterized by TOF are essential for this project. It is desirable for TOF measurements to have crystals that grow with a platelet motif and to have thick crystals with parallel surfaces. Thicker crystals provide a large transport distance allowing the width of the current pulse to sufficiently broaden during the movement

across the crystal. This allows for the observation in the variation of drift velocities through the crystal providing a representative view of the intrinsic factors controlling transport within the crystal. It also provides a better statistical measurement of the transit time. Typical crystal thicknesses grown in this study are in the range of 100 μm. Crystals with defect free surfaces are also desirable for lateral field TOF.

The discussion below focuses on crystal growth by horizontal physical vapor transport (PVT).[127] The crystal growth efforts for this project focused on this technique because this method has been shown to yield high purity and highly ordered single crystals.[128] In the PVT growth technique, the starting material is sublimed in a closed quartz tube in a flow of high purity carrier gas, namely high purity argon in this work. A schematic of the PVT crystal growth process is shown in Figure 5.1. The actual growth setup is shown in Figure 5.2. The basic setup consists of, from outer shell to inner: 1) an outer glass insulation tube that acts as the system support structure, 2) an inner insulation tube that supports the heating rope for the hot zone, 3) a gas flow tube, that supports the heating wire, is sealed at the ends by ground-glass joints with tubing connectors to allow the transport of the carrier gas, 4) a crystal growth tube where the crystal growth occurs and 5) a source tube that holds the starting material. The starting material is loaded in the source tube which is placed in the hot zone in the region of the heating rope and the temperature is adjusted to cause the starting material to sublime. The carrier gas transports the sublimed material down the growth through a temperature gradient as shown in Figure 5.1. The temperature gradient is created using resistive heating by adjusting the current through the heating rope (Omega, part # FGR-060)

located in the area of the hot zone and the current through the resistance heating wire (Omega Engineering, part # NI80-032-50) which is wrapped the entire length of the inner gas flow tube. The temperature gradient is adjusted to realize a temperature zone where the pure material grows in single crystals near the middle of the growth tube. Heavier molecular weight impurities, which sublime at higher temperatures, remain in the high temperature region and lighter molecular weight impurities, which recrystallize at lower temperatures, deposit in the low temperature region. High purity single crystals then deposit in the optimized crystal growth zone.

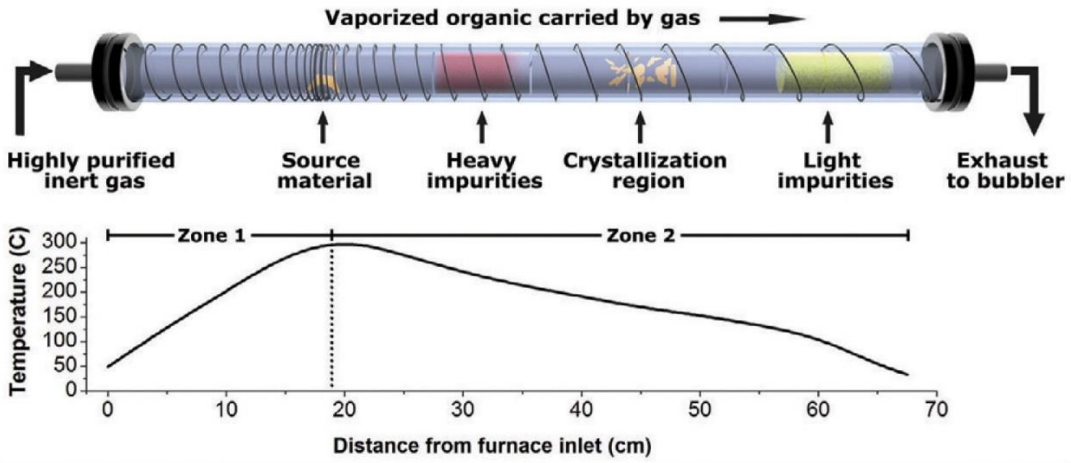

Figure 5.1: Upper: General schematic of the horizontal physical vapor transport crystal growth setup**.** Lower: Temperature gradient typical for growth of rubrene single crystals.[23] Reprinted with permission. Copyright 2007 Elsevier.

Single crystals of tetracene and rubrene were grown for this work. The source material for the crystal growth was 98% pure tetracene and 98% pure rubrene which were purchased from Sigma-Aldrich. About 400-500 mg of starting material was

typically loaded in the high temperature end of the crystal growth setup. A sublimation temperature of 175º C was used for tetracene and 285º C for rubrene. Three thermocouples (K-type, Omega Engineering, part # 5SC-GG-K-30-36) were used to monitor the temperature along the growth tube and were placed in the hot zone (under the heating rope), in the middle of the growth tube and towards the low temperature end. The temperature gradient was kept as steep as possible along the growth tube to keep the growth deposition zone in a narrow range to grow larger crystals. High purity argon was used as a carrier gas and was bubbled through mineral oil after passing through the growth setup. The argon gas flow rate was typically 60 bubbles per minute (approximately 2.6 mL/min).

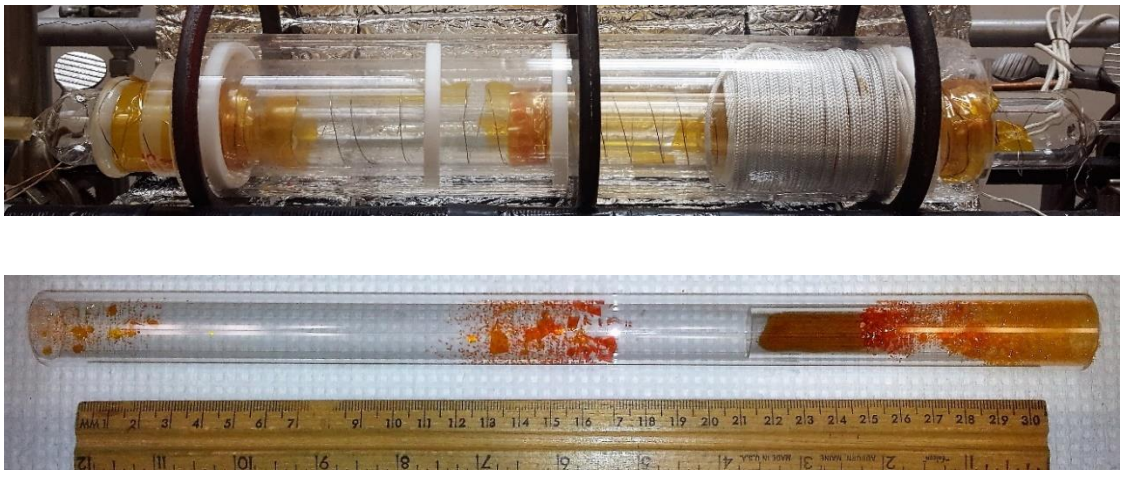

Figure 5.2: Upper: PVT crystal growth apparatus assembled. Lower: Growth tube with tetracene crystals located in the center region. Gas flow from right to left in both images.

The progress of the crystal growth was monitored throughout the growth process. Growth times varied, but were sometimes longer than four weeks if good quality crystals were observed growing. Figure 5.2 shows a typical growth tube after crystal growth. Note the grouping of crystals in the middle of the tube. Figure 5.3 shows typical tetracene and rubrene crystal growths after they were harvested.

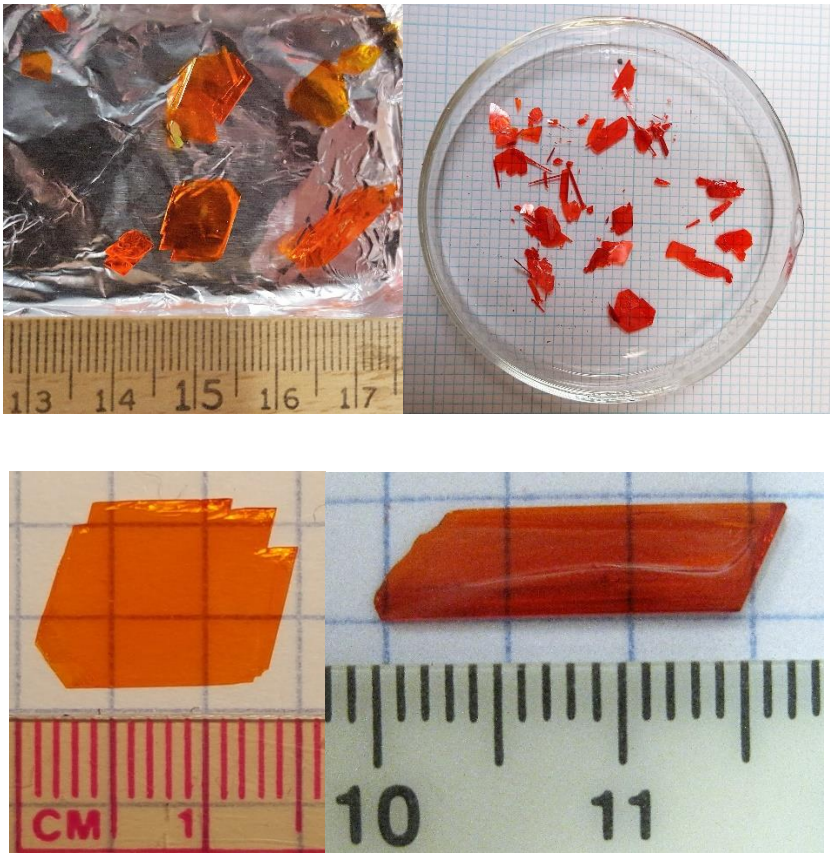

Figure 5.3: Single crystals gown by PVT. Tetracene: left images. Rubrene: right images.

5.1.2 Evaluation of Single Crystals

After crystal growth, the crystals were carefully harvested. The crystals were inspected under an optical microscope to check for any obvious signs of cracking, stress or other imperfections. The selected crystals were then checked for twinning using an optical microscope using crossed polarizers. Crystals of conjugated molecules are typically birefringent and individual crystals will have a strong color contrast when oriented in different directions under crossed polarizers.[129] This allows the selection of crystals with a single crystalline structure. Figure 5.4 shows a rubrene crystal analyzed through crossed polarizers.

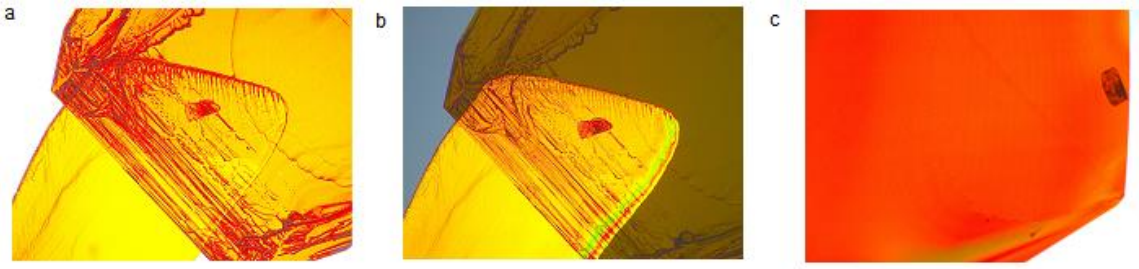

Figure 5.4: Rubrene crystals examined using cross polarized light microscope (4x). a) Unpolarized light. b) Under cross polarized light showing crystal twinning. c) Under cross polarized light showing a single crystal with a small imperfection.

5.1.3 Single Crystal Sample Preparation

After crystal selection, metal contacts were deposited on opposing planar surfaces (for vertical TOF) and on the same surface (for lateral TOF). Ag metal contacts were deposited using a Denton Desk IV sputter coater. Contact size and spacing was controlled using a shadow mask. The thickness of the contact for vertical TOF was such that it was transparent to the excitation source used to create the electron hole pair but thick enough to show good conductivity. Contact thicknesses for Ag contacts in the range of 20 nm provided these conditions. Crystal thicknesses were measured after the vertical TOF measurement by cleaving the crystal perpendicular to the surface through the contact area and measuring the crystal thickness using a calibrated optical microscope or a scanning electron microscope.

5.2 Instrumentation Design - Vertical TOF

For vertical (bulk) TOF measurements, crystals were mounted on a copper plate that serves as a support electrode. A small amount of Ag paste was applied between the sputtered portion on the bottom of the crystal and the copper support plate to ensure good electrical contact. This assembly was then mounted on the bottom electrode using silver paste which was attached to the cold head of the cryostat as discussed in more detail below and shown in Figure 5.5. The top electrical contact was made by applying

a small amount of Ag paste to the tip of a copper wire (30 AWG) which was then attached to the sputter contact of the crystal. The copper wire was then attached to the upper contact which was connected to the TOF remaining circuit.

The sample stage for the vertical TOF analysis was a home-made stage built on the cold head of a RMC-Cryosystems closed cycle He cryostat as shown in Figure 5.5. A 2 mm thick piece of borosilicate glass was cut to fit on the top of the copper cold head to provide electrical insulation. The glass was mounted to the cold head using Apiezon N grease. Apiezon N grease provided crack free structural stability well below the temperatures we investigated and also provided good thermal transport at low temperatures. The electrodes where constructed of copper sheet approximately 1mm thick. The lower contact was bent in an L shape to allow electrical lead attachment to an attached screw that provided contact to the remaining circuit. The upper contact was a small piece of copper plate with two crews to allow lead attachment. Both copper electrodes were pasted to the glass for stability using Stycast 2850T epoxy (Lake Shore Cryotonics). Electrical leads from the contacts to the cryostats electrical feedthroughs were made with coaxial cable (Part # CC-SC-25, Lake Shore Cryotonics). The temperature of the sample mount was monitored using a Si diode sensor (Model DT-670C-SD and DT-471-CO, Lakeshore Cryotronics) mounted on the glass substrate using Apiezon N.

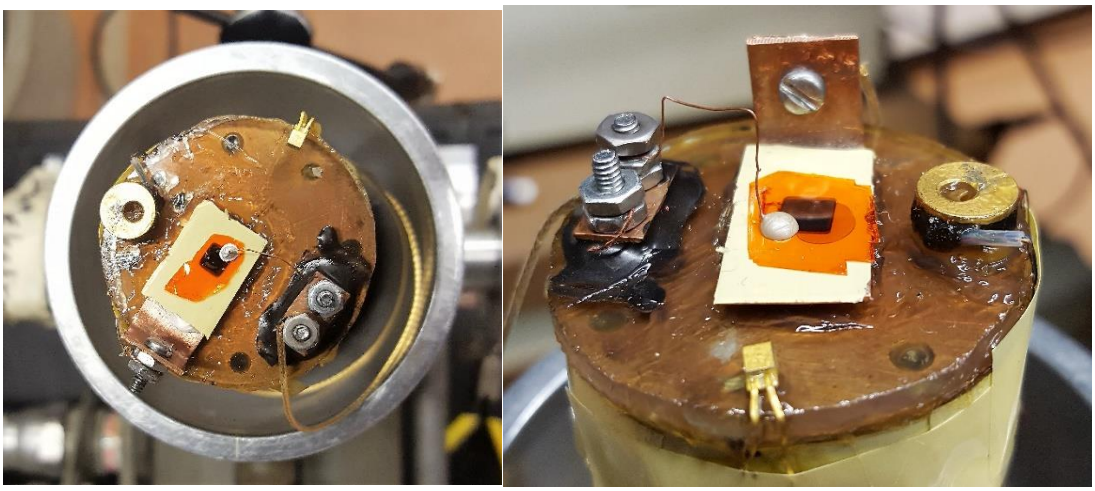

Figure 5.5: Sample mount on cryostat cold head for vertical TOF analysis. Tetracene crystal shown. Description of sample mount in text.

A Photon Technology International GL-3300 nitrogen laser (337 nm, pulse width of 800 ps) with random polarization was used to create charge carriers in the sample. The crystals were excited at normal incidence to the **a-b** crystal facet for both vertical and lateral TOF. The intensity of the laser pulse was adjusted using neutral density filters to ensure no internal space charge effects were encountered due to excessive charge carrier density. Tetracene and rubrene crystals have a high optical absorbance with an absorption coefficient greater than $1x10^4 cm^{-1}$ at 337 nm resulting in an absorption length of less than 1 μm.[130] DC voltage was applied to the crystal using a Keithly 2410 Sourcemeter. The TOF photocurrent transient was measured as a voltage drop across a 1 kΩ resistor using a Tektronix DPO7104 1 GHz oscilloscope (Figure 5.6). Crystals were examined as a function of applied voltage at constant temperature (296 K) or as a function of temperature (140–296 K) at constant voltage.

Figure 5.6: Instrumentation used in vertical and lateral TOF.

5.3 Instrumentation Design - Lateral Field TOF

In an attempt to characterize charge transport properties that take place on or near the crystal surface, Lateral Field Time of Flight (LFTOF) was investigated. The approach utilized a microscope objective design and was constructed similar to the setup used by Isberg.[119] A schematic of the general LFTOF circuit that is used is shown in Figure 5.7.

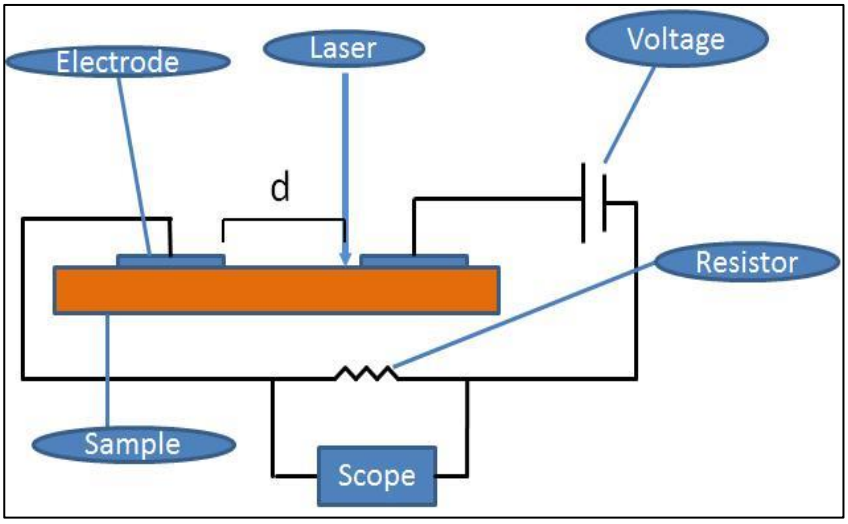

Figure 5.7: Schematic of a LFTOF circuit.

Samples were prepared for LFTOF, by mounting crystals on a glass slide using double sided tape. Two contacts were sputtered on the upper crystal surface as shown in Figure 5.8 using a shadow mask as described earlier. The distance between contacts were measured using an optical microscope. The glass slide was then mounted to a x,y,z translation stage. Electrical contact was made to each sputtered contact using silver paste.

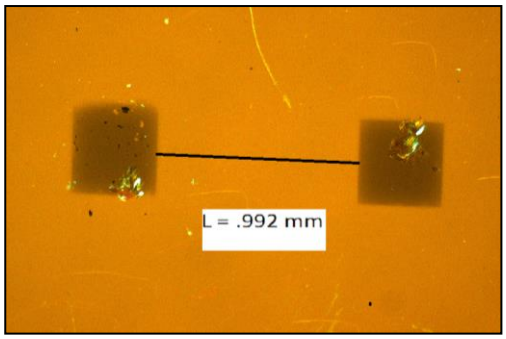

Figure 5.8: Surface of a tetracene single crystal with sputtered contacts for LFTOF**.**

A pulsed nitrogen laser was used as an excitation source and was guided into the experimental setup and focused onto the sample with a UV objective (15X/.28NA HP Reflx, Infinite conjugated, Edmund Scientific). The objective has a resolution of about 0.73 μm at the laser's wavelength (using resolution = 0.61λ/NA). A cylindrical lens was used before the objective to focus the beam to a line. Electron-hole pairs were generated on or near the sample surface upon illumination. By adjusting the intensity of the laser using neutral density filters, the depth and number of carriers generated can be adjusted.

The nitrogen laser was passed through the optical setup and focused on the sample by the objective, Figures 5.9 and 5.10. The sample surface was imaged by the objective. The beam-splitter redirects the image horizontally where it was imaged by the CCD camera. The laser spot size was adjusted to around 10 microns. This laser spot could be moved to different locations between the sputtered contacts to change the distance traveled by the generated carriers.

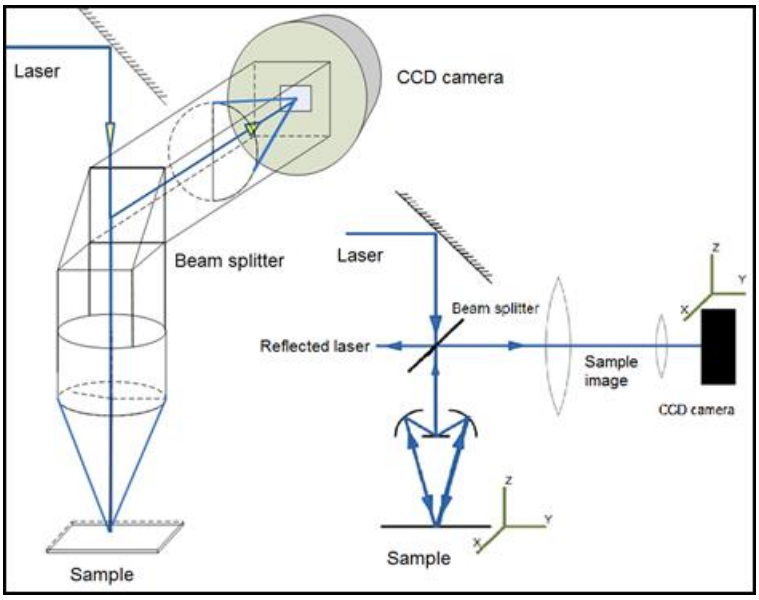

Figure 5.9: 3-D and 2-D Schematic of optical path LFTOF system.

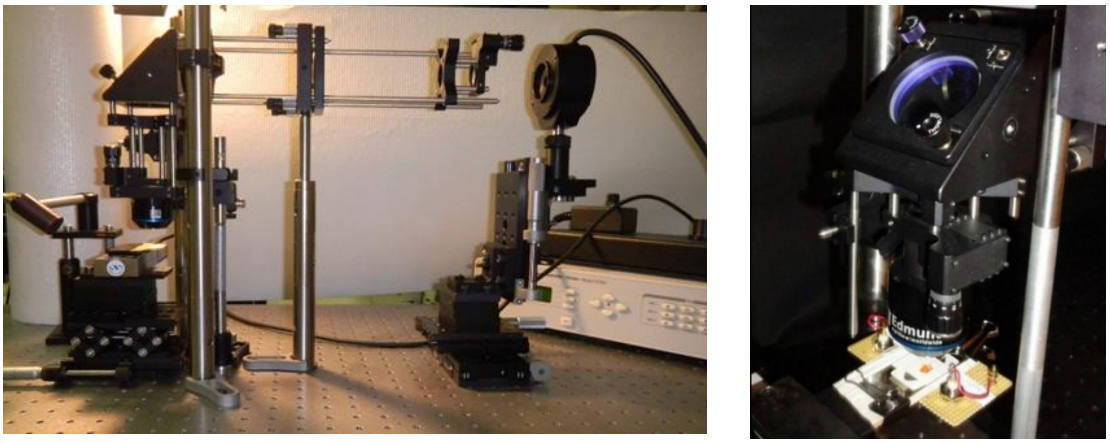

Figure 5.10: Lateral field time-of-flight system. Left image shows optical path with CCD camera to the right and sample stage to the left. Right image shows focusing optics and sample stage with mounted crystal. See Figure 5.9 for components.

Chapter 6

TOF Experimental Results

In this chapter, experimental results of TOF investigations of the charge carrier hole mobilities in the bulk of tetracene and rubrene single crystals and on the surface of tetracene single crystals are presented. Room temperature mobilities, low temperature mobilities, as well as mobility as a function of voltage are examined. The chapter starts with the initial vertical TOF work on tetracene single crystals to establish the techniques and instrumentation employed and to gain experience with the experimental process. This is followed by more extensive vertical TOF work on rubrene single crystals which includes low temperature measurements. The chapter concludes with a discussion of initial work on tetracene lateral field TOF measurements. Experimental details and instrumentation descriptions are discussed in the previous chapter.

6.1 Tetracene – Vertical TOF

This work involved establishing a laboratory capable of doing TOF measurements at St Cloud State University (and in collaboration with the University of Minnesota). In doing so, it was desirable to start with a material that had been studied previously to demonstrate the ability to perform these measurements. Tetracene was chosen as an initial material because single crystals of tetracene are relatively easy to grow using the PVT technique and TOF hole mobility results have been previously reported.[131-133]

TOF results as a function of voltage at room temperature for a single crystal of tetracene in the **c**-direction are shown in Figure 6.1a. Results are given for voltages ranging from 500V – 800V. Below 500V the signal had too much noise to be able to determine a reasonable transit time. Above 900V the signal narrowed to a point that a distinct plateau in the log-log plot could not be realized. This narrowing effect can be seen in the TOF signal at 800V in Figure 6.1a. Figure 6.1b shows the log-log plot of the signals from Figure 6.1a. A clearer picture of the transit time can be given by drawing asymptote lines through the plateau and the slope of the shoulder as shown in Figure 6.3b. The log-log plots of Figure 6.1b show a steady decrease in the transit times with increasing voltage as would be expected. Transit times and calculated hole mobilities for each voltage are given in Table 6.1 and show good consistency. Figure 6.2 shows the plot of the inverse transit times vs electric field and demonstrates the

linear relationship between the two for the given voltages. The slope of this line can be used to calculate the mobility.

The calculated TOF hole mobility for the tetracene crystal from Figure 6.2 was 1.3 ± 0.05 cm^2/Vs. This value is in line with previous reported TOF hole mobilities in the **c**-direction for sublimation grown tetracene crystals at room temperature. Niemax *et al.*[131] reported an average value of 1 cm^2/Vs, de Boer *et al.*[132] reported values from $0.5 – 0.8$ cm^2/Vs for three crystals and Berrehar *et al.*[133] reported an average value of 0.85 cm^2/Vs. Variations in the reported values between labs could be in part explained in the growth quality and preparation of the crystal. Handling of the crystal could result in residual strains throughout the crystal that may not be detected using polarized light or XRD.[134] Even though our reported data are somewhat higher and represents only one crystal, they demonstrated that our experimental techniques and instrumentation design were sound.

Low temperature measurements (< 300K) were also performed on tetracene single crystals but resulted in a very dispersive signal that did not allow for the determination of the transit time. This observation was also reported by de Boer *et al.*[132] for temperatures below room temperature, where they observed a 'blurring of the TOF pulse'. Additional work is planned to investigate possible techniques to allow for acquisition of TOF signals below room temperature for tetracene.

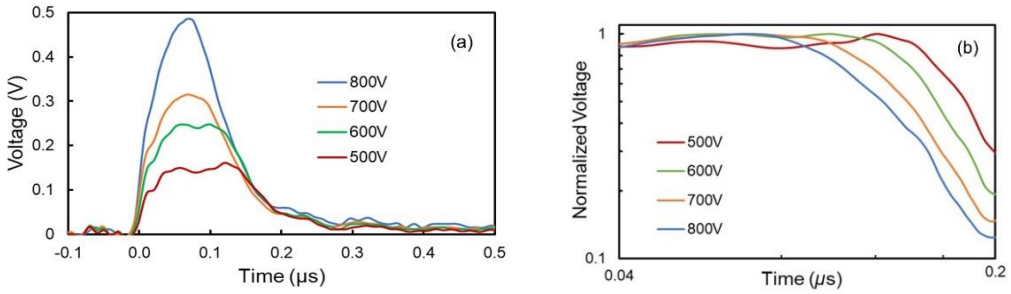

Figure 6.1: TOF hole signal obtained from tetracene crystal (**c**-direction) (a) as a function of voltage. (b) log V vs. log t TOF pulses from tetracene crystal in Figure 6.1a. L=100 μm, 296 K. Transit times: 500 V, t_{tr} = 0.147 μs; 600 V, t_{tr} = 0.129 μs; 700 V, t_{tr} = 0.114 μs; 800 V, t_{tr} = 0.099 μs.

Voltage (V)	**Transit time (μs)**	**Hole Mobility (cm^2/Vs)**
500	0.147	1.36
600	0.129	1.29
700	0.114	1.26
800	0.099	1.26

Table 6.1: Calculated hole mobilities from tetracene crystal of Figure 6.1.

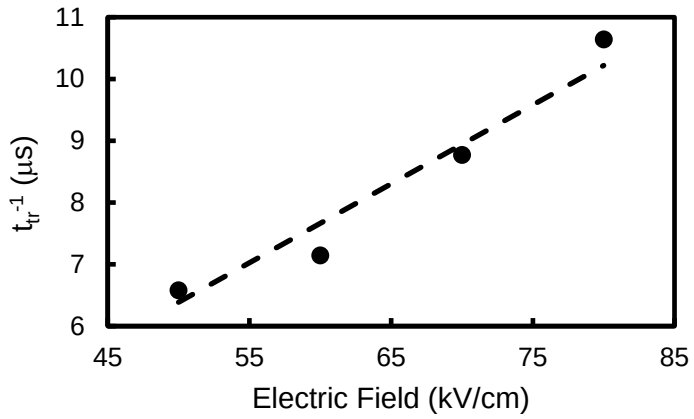

Figure 6.2: Room temperature inverse transit times vs electric field for tetracene crystal**.** L = 100 μm, V = 500-800 V, E = 50-80 kV/cm. Slope = μ/L = 128 cm/Vs. Calculated mobility from the slope, μ = 1.3 cm^2/Vs.

6.2 Rubrene – Vertical TOF

A major portion of this work involved the characterization of the hole mobilities in the **c**-direction in rubrene by vertical TOF. The crystal structure of rubrene is given in Chapter 2. This includes measurements as a function of electric field (43–79 kV/cm) and as a function of temperature (140–300 K). Rubrene (5,6,11,12-tetraphenyltetracene) has been well characterized by field effect measurements in the **a** and **b** crystal directions[28, 38, 135] and has shown the highest measured room temperature field effect hole mobilities of oligoacene single crystals studied to date with a reported hole mobility of 20 cm^2/Vs at 300 K in the **b**-axis direction.[38] Very little work has been reported on the determination of hole mobilities in the **c**-axis direction for rubrene. In much older work, Williams[136] reported TOF results for rubrene single crystals in the **c**-axis direction of 0.5 cm^2/Vs at room temperature with mobilities increasing to 2 cm^2/Vs at 473 K. Subsequent to the work described here, Blülle *et al.*[73] reported low temperature hole mobility measurements in rubrene single crystals, using high-frequency admittance spectroscopy, of 0.2 cm^2/Vs at 300 K increasing to around 0.8 cm^2/Vs at 175 K.

Field effect mobility measurements have demonstrated the anisotropic nature of charge transport in the **a**-**b** surface plane of rubrene with reported hole mobilities in the

b-axis direction being three times larger than in the **a**-axis direction. These field effect measurements also showed band-like hole transport in both the **a** and **b** directions upon cooling from 300 K to 150 K with a sudden decrease in mobility occurring at 150 K.

6.2.1 Room Temperature and Voltage Dependent Measurements

In this study, we report vertical TOF hole drift mobility measurements in the **c**-axis direction obtained from five different rubrene single crystals as a function of temperature and electric field. Mobility measurements were conducted at room temperature under atmospheric conditions and at low temperature in a He cryostat at a vacuum of 50 mTorr. Table 6.2 shows the observed room temperature hole mobility values for the five individual rubrene crystals for the given conditions.

Crystal	Source	Mobility (cm^2/Vs)
1	Atmospheric (Fig. 6.3)	0.37
2	Voltage bias data (Fig. 6.4)	0.24
3	Cryostat (50 mTorr)	0.27
4	Cryostat (50 mTorr)	0.27
5	Cryostat (50mTorr)	0.31

Table 6.2: Rubrene room temperature TOF mobilities (296 K) from five different rubrene crystals under different conditions.[35] Reprinted with permission. Copyright 2015 AIP Publishing.

A typical TOF hole pulse for a rubrene crystal (crystal 1) at room temperature and atmospheric conditions is shown in Figure 6.3a. The location of the transit time, t_{tr}, is

noted. Figure 6.3b gives the resulting log V – log t plot with asymptotes drawn from the plateau and the tail. The intersection of the asymptotes is taken to be the transit time. The room temperature mobility from this crystal was calculated to be 0.37 cm^2/Vs.

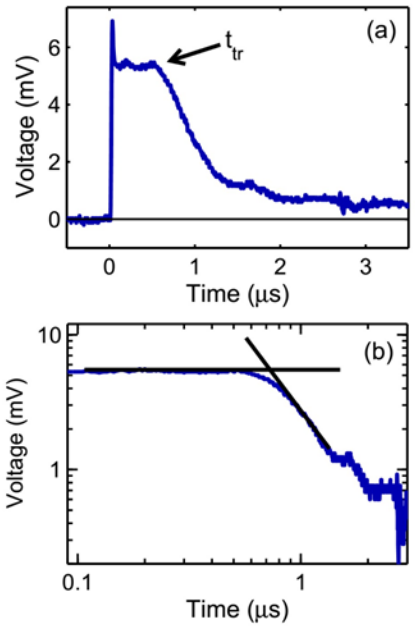

Figure 6.3: (a) TOF hole signal obtained from rubrene crystal 1. T = 296 K, L = 145 μm, V = 800 V, E = 55 kV/cm, t_{tr} = 0.71 μs, μ = 0.37 cm^2/Vs. Transit time noted as t_{tr}. (b) Log V versus log t plot of Figure 6.3a. Intercept of asymptotes represents t_{tr}.[35] Reprinted with permission. Copyright 2015 AIP Publishing.

The voltage dependence of the hole mobility in crystal 2 was examined with the applied voltage being varied from 600-1100 V and resulting electric fields (E) of 43-79 kV/cm. The plot of the linear relationship between the inverse transit time vs the electric field is given in Figure 6.4. This linear relationship allows the mobility to be determined

using the slope of the plot and the crystal thickness. The room temperature mobility for crystal 2 was calculated from this data to be 0.24 cm^2/Vs.

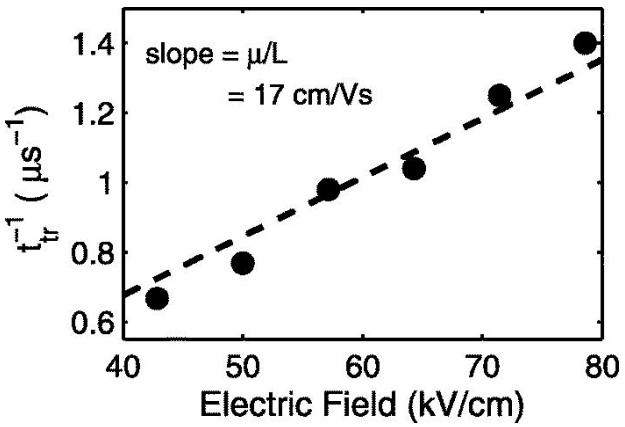

Figure 6.4: Voltage dependence of transit time from rubrene crystal 2. L = 140 μm, V = 600–1100 V, E = 43–79 kV/cm. Slope = 17 cm/Vs. Calculated hole mobility, μ = 0.24 cm^2 /Vs.[35] Reprinted with permission. Copyright 2015 AIP Publishing.

6.2.2 Low Temperature Measurements

Of particular interest in this study was the low temperature-mobility relationship. The mobility of three different rubrene crystals were measured as a function of temperature. Figure 6.5 shows a TOF hole pulse at three different temperatures for crystal 5. The voltage scale has been offset to better visualize the decrease in transit time with decreasing temperature. Figure 6.5 also shows the log V - log t plot as a

function of temperature which demonstrates the decreasing transit time with decreasing temperature. For crystal 5, the mobility increased with decreasing temperature, increasing from 0.31 cm^2/Vs at 296 K to 0.84 cm^2/Vs at 180 K. Crystals 3 and 4 were also studied as a function of temperature and their mobilities as a function of temperature are shown in Figure 6.6a. Crystals 3 and 4 showed a similar trend with increasing mobility with decreasing temperature. Crystals 3 and 4 also showed a decrease in mobility below 180 K similar to that observed for low temperature FET measurements in the **a** and **b** axis of rubrene.[38] Crystal 5 cracked during measurements at around 180 K and thus no data was collected below 180 K. The mobilities for all three crystals studied at low temperature are in good agreement with an average mobility at 180 K of 0.70 ± 0.12 cm^2/Vs.

The three crystals measured at low temperature exhibited an inverse power law dependence, $\mu = \mu_0 T^{-n}$, where n = 1-3, in the range of 296 – 180 K. This relationship can be seen in 6.6b with an average value of $n = 1.8 \pm 0.2$ for the three crystals. This value of n compares nicely with a result of n = 2 which was determined over the same temperature range in the conduction channel of a rubrene single crystal FET using Hall effect measurements.[59] It also is in close agreement with computational results of n = 2.1 reported by Troisi[99] for a rubrene crystal over the same temperature range.

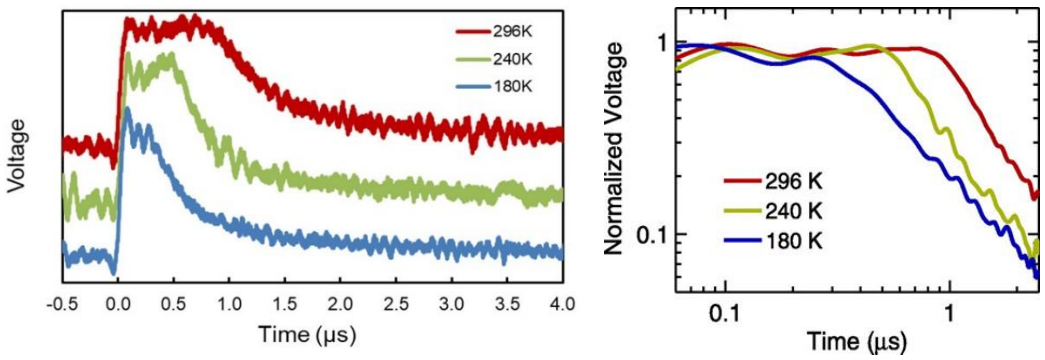

Figure 6.5: Left: TOF hole signals as a function of temperature for rubrene crystal 5. Voltages are offset. Right: Temperature dependent log V vs. log t TOF pulses from Crystal 5. L = 105 μm, V = 400 V, E = 38 kV/cm. 298 K; t_{tr} = 0.88 μs, μ = 0.31 cm^2/Vs. 240 K; t_{tr} = 0.52 μs, μ = 0.53 cm^2/Vs. 180 K; t_{tr} = 0.33 μs, μ = 0.84 cm^2/Vs.[35] Reprinted with permission. Copyright 2015 AIP Publishing.

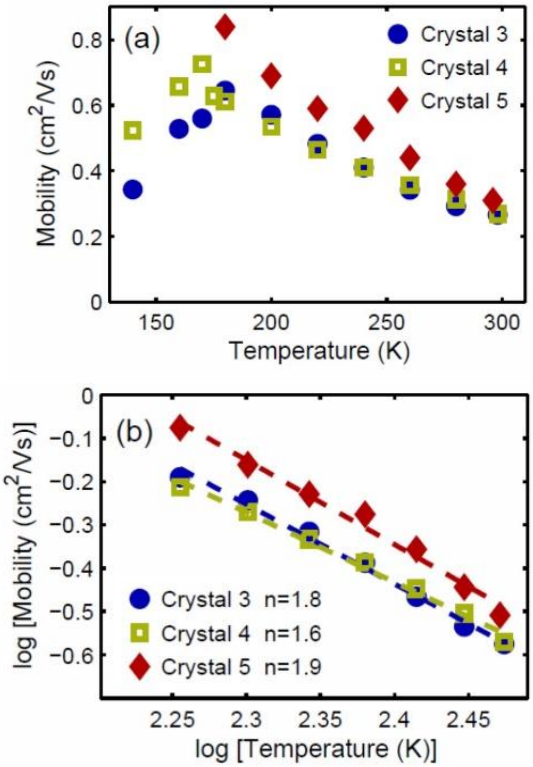

Figure 6.6: (a) Temperature dependence of bulk TOF hole mobilities for rubrene crystals 3, 4, and 5. V = 400 V. (b) Log-log plot of the mobility data in the inverse power law transport region (T = 180-296 K). Dashed lines show linear fits to the log-log data: $\log(\mu) = \log(\mu_0) - n\log(T)$.[35] Reprinted with permission. Copyright 2015 AIP Publishing.

6.2.3 Rubrene TOF Discussion

The hole mobility data collected helps confirm the anisotropic charge transport in rubrene single crystals showing an almost hundredfold difference between the TOF mobility measurements in the **c**-axis direction (~ 0.3 cm^2/Vs) and the FET measurements in the **b**-axis direction (~ 20 cm^2/Vs). This anisotropic nature is expected from quantum mechanical calculations that indicate that the transfer integrals are much weaker in the **c**-axis direction.[48]

These measurements also showed low temperature power law dependence with an increase of mobility with decreasing temperature. This power law dependence is taken to be a sign of "band-like' transport. It should be noted, that Karl also reported "band-like" transport for TOF mobilities along the **c**-axis of anthracene.[109] But as was discussed in Chapter 3, band-like transport is not a valid explanation for charge transport mechanisms in these organic single crystal semiconductor materials which seem to be dominated by dynamic disorder due to large crystal thermal molecular motion that disrupts the molecular lattice. In the new train of thought for charge transport mechanisms, band-like transport has been supplanted by the concept of transient localization. However, this does not explain the transport observed in the **c**-axis direction. As proposed by Blulle *et al.*[73], the transport in the **ab** crystal plane is decoupled from the transport in the **c**-axis direction. This decoupling can be explained by looking at the timescale of the transport in the **c**-axis direction as compared to the

timescale of the transport in the **ab** crystal plane. Transport in the **ab** plane can be thought of as being coherent transport but modulated by low frequency molecular motion with the resulting fluctuations in the transfer integral being on the timescale of ~ 1ps. The mobility in the **c**-axis direction is much slower and can be considered to follow an incoherent hopping transport model. The room temperature hopping time can be estimated using Einstein's relation. Given a hole mobility in the **c**-axis direction of $\mu \sim 0.2$ cm^2/Vs and an **ab** interlayer distance of 13.5 Å, the calculated room temperature hopping time between layers in the **c**-axis direction is ~ 3 ps.[73] Even though we can describe the transport between the **c**-axis direction and the **ab** plane as being decoupled, they can be thought to be related through the amount of charge carrier delocalization in the **ab** plane. As a carrier becomes more delocalized, the more loosely held it can be considered to be, and thus there is a higher probability of incoherent hopping between the **ab** crystal planes representing the transport in the **c**-axis direction. This was discussed in more detail in Chapter 3 and the results of our measurements in the **c**-axis direction tend to follow this proposed model.

6.3 Lateral Field TOF

This section contains preliminary, proof of concept, results of LFTOF measurements that were collected to demonstrate the potential effectiveness of its use in the characterization of charge transport properties on the surface of single crystals of

oligoacene semiconductor materials. This is not a complete data set but provides a starting point for future work.

These initial measurements were made on the surface of a tetracene single crystal and the experimental design was discussed in the previous chapter. The crystal surface orientation was not taken in to account in this study. Previous FET measurements showed anisotropic mobility behavior along the surface on tetracene crystals.[36] Two experimental parameters were investigated to determine if the observed LFTOF results followed expected or intuitive outcomes. The first area investigated was the amount of laser flux on the surface of the crystal and the potential for oversaturation and/or creation of excess charge carriers. The second area investigated was the effect of the applied voltage on the carrier transit time.

6.3.1 LFTOF - Excitation Energy Dependence

Lateral field TOF data was collected as a function of transmission (%T) of the laser flux to examine the effect of the excitation energy on the resulting TOF signal. Neutral density filters were used to decrease the laser flux on the crystal surface. The nitrogen laser used has an output energy of 1.69 mJ per pulse at 3 Hz. The output power was not measured at the sample. Five different optical flux densities were examined. Three with high transmission, 100 %T (no filter), 91 %T and 79 %T and two with low transmission, 10 %T and 0.1 %T. LFTOF hole signals obtained from the surface of a

tetracene single crystal for the five different %T are shown in Figure 6.7. Transit times, signal voltages measured at 0.25 μs and calculated hole mobilities for the 5 signals are given in Table 6.3 with an average value of 0.78 cm^2/Vs..

The measured signal voltages, which can be related to the photocurrent, showed an approximate linear relationship, Figure 6.8, while taking into account the noise levels of the signals. These results follow previous studies that found the generated photocurrent in tetracene, j, is proportional to the intensity of the excitation light, I_0, where $j \propto I_0^n$, with n ≈ 1 at excitation wavelengths around 337 nm and high electric fields.[137-138]

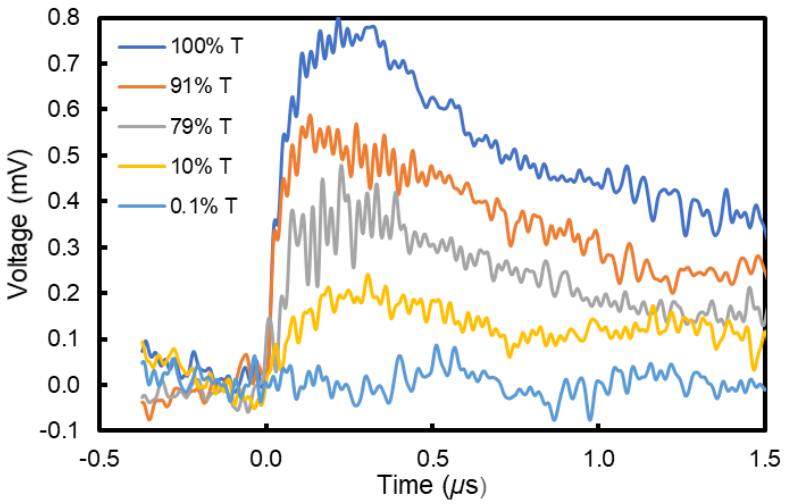

Figure 6.7: LFTOF hole signal obtained from surface of a tetracene single crystal as a function of laser flux controlled using optical filters (%T). V = 1000 V. L = 150 μm. 296 K.

The LFTOF voltage signals showed a slight dispersive character with a higher baseline after the signal pulse with increasing laser flux. This could indicate an

increased number of charge carriers being created in the vertical direction deeper into the crystal. One could expect that the carriers would see a different molecular structure including the density of trap states from the surface to a distance below the surface of the crystal. This would result in different carrier dynamics that could spread the range of transit times observed.

Filter (%T)	V at 0.25 μs (mV)	Transit Time (μs)	Hole Mobility (cm^2/Vs)
100 (no filter)	0.78	0.326	0.86
91	0.54	0.369	0.76
79	0.37	0.366	0.77
10	0.18	0.394	0.71
0.1	0	N/A	N/A

Table 6.3: LFTOF data from Figure 6.7. Signal voltage for different %T signals measured at 0.25 µs. Signal pulse transit times and calculated hole mobility. V = 1000V. L = 150 µm. 296 K.

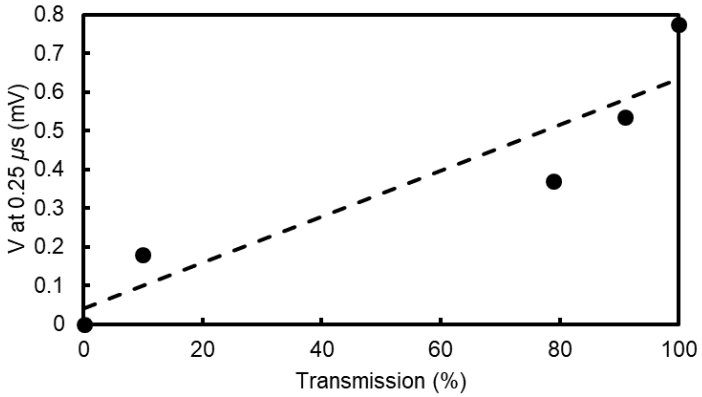

Figure 6.8: LFTOF signal voltage versus transmission (%) from signals in Figure 6.7 and data in Table 6.3. Trend line is for the eye only.

6.3.2 LFTOF - Voltage Dependence

The voltage dependence of the hole mobility was examined with the applied voltage being varied from 800-1100 V and resulting electric fields (E) of 53-73 kV/cm. LFTOF hole voltage plots for 800 V and 1100 V are shown in Figure 6.9 with the corresponding log V: log t plot shown in 6.10. The results showed a decrease in transit time with increasing voltage as would be expected as noted in Table 6.4. This demonstrates a linear relationship between the electric field and the applied voltage, E = V/L, where L in the carrier transport distance across the crystal surface. The plot of the inverse transit times vs electric fields is shown in Figure 6.11. The hole mobility calculated from the slope of this plot is 0.81 cm^2/Vs.

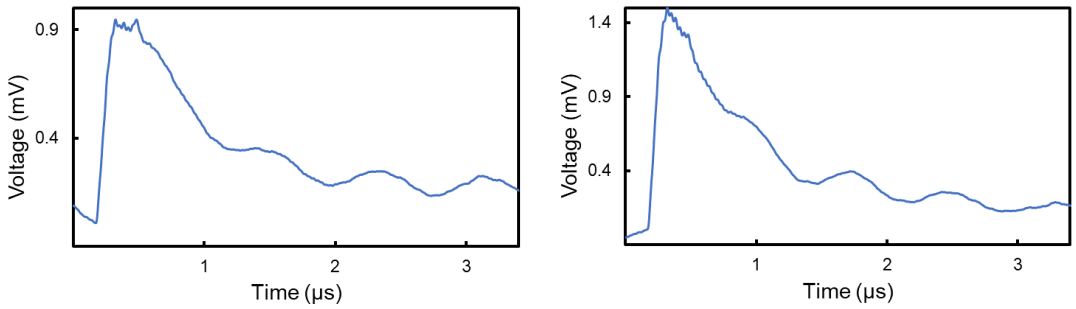

Figure 6.9: LFTOF hole signal from tetracene single crystal surface. Left: V = 800V. Right: V = 1100V. T = 296K. L = 150 μm. 100 %T. Transit times and mobility are listed in Table 6.4.

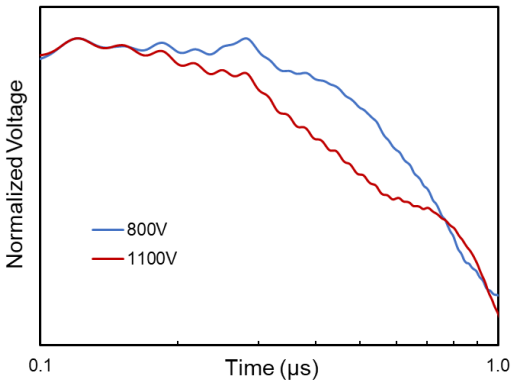

Figure 6.10: Normalized log V versus log t of LFTOF signals from Figure 6.9 showing a decrease in transit times.

Voltage (V)	Transit Time (μs)	Hole Mobility (cm^2/Vs)
800	0.337	0.83
900	0.295	0.85
1000	0.271	0.83
1100	0.271	0.76

Table 6.4: Voltage, transit times and hole mobility from tetracene single crystal surface**.** L = 296K. L = 0.015 cm.

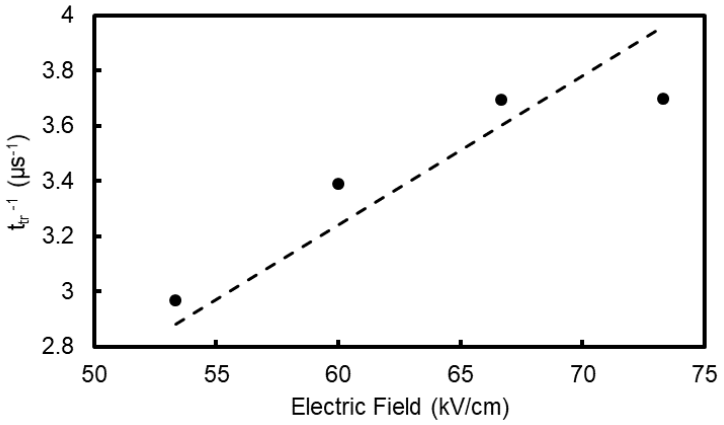

Figure 6.11: Electric field dependence of transit time from LFTOF of tetracene crystal data from Table 6.4. L = 150 μm, V = 800 – 1100 V, E = 53 -73 kV/cm. Slope = μ/L =54 cm/Vs. Calculated mobility, μ = 0.81 cm^2/Vs.

6.3.3 LFTOF Discussion

Laser flux experiments resulted in a linear relationship between the TOF signal voltage and the laser intensity. This demonstrated that charge carrier creation on the surface is possible without saturation of the signal at the wavelength and power levels used. Voltage dependent measurements showed a decrease in transit time with increasing voltage giving consistent mobilities throughout the voltage range as would be expected in a typical TOF experiment. The experimental LFTOF parameters investigated produced positive results indicating the instrumental design put forward can provide reliable carrier mobility measurements.

The LFTOF data reported above yielded hole mobility values of around 0.8 cm^2/Vs. These compare with reported FET mobilities in the range of 0.4 – 1.6 cm^2/Vs [36, 39, 139] which represents a small sampling of published FET results. The LFTOF values are within the range of the FET measurements conducted with tetracene single crystals which provides a reasonable evaluation of the validity of the proposed method. This creates a good foundation for further investigation of the LFTOF technique for determination of charge carrier mobilities on the surface of single crystal organic semiconductors.

References

1. Ahmad, S., Organic Semiconductors for Device Applications: Current Trends and Future Prospects. *J. Poly. Eng.* **2014,** *34* (4), 279-338.

2. Shirota, Y.; Kageyama, H., Charge Carrier Transporting Molecular Materials and their Applications in Devices *Chem. Rev.* **2007,** *107* (4), 953-1010.

3. Friend, R., Organic Materials for Large Area Electronics. *Mats. Sci. Forum* **2009,** *608*, 159-179.

4. Root, S. E.; Savagatrup, S.; Printz, A. D.; Rodriquez, D.; Lipomi, D. J., Mechanical Properties of Organic Semiconductors for Stretchable, Highly Flexible and Mechanically Robust Electronics. *Chem. Rev.* **2017,** *117* (9), 6467-6499.

5. Marrocchi, A.; Faacchetti, A.; Lanari, D.; Petrucci, C.; Vaccaro, L., Current Methodologies for a Sustainable Approach to π-Conjugated Organic Semiconductors. *Energy Environ, Sci.* **2016,** *9* (3), 763-786.

6. Sen, H.; Di, C.-A.; Zhu, D., Organic Transistor for Bioelectronic Applications. *Sci. China Chem.* **2017,** *60* (4), 437-449.

7. Sevilla, G. A. T.; Hussain, M. M., Printed Organic and Inorganic Electronics: Devices to Systems. *IEEE J. Em. Sel. Top. C* **2017,** *7* (1), 147-160.

8. Ward, J. W.; Lamport, Z. A.; Jurchescu, O. D., Versatile Organic Transistors by Solution Processing. *ChemPhysChem* **2015,** *16* (6), 1118-1132.

9. Simon, D. T.; Gabrielsson, E. O.; Tybrandt, K.; Berggren, M., Organic Bioelectronics: Bridging the Signal Gap Between Biology and Technology. *Chem. Rev.* **2016,** *116* (21), 13009-13041.

10. Mei, J.; Diao, Y.; Appleton, A. L.; Fang, L.; Bao, Z., Integrated Materials Design of Organic Semiconductors for Field-Effect Transistors. *J. Am. Chem. Soc.* **2013,** *135* (18), 6724-6746.

11. Sirringhaus, H., 25th Anniversary Article: Organic Field-Effect Transistors: The Path Beyond Amorphous Silicon. *Adv. Mater.* **2014,** *26* (9), 1319-1335.

12. Usta, H.; Faacchetti, A., Polymeric and Small-Molecule Semiconductors for Organic Field-Effect Transistors. In *Large Area and Flexible Electronics*, Caironi, M.; Noh, Y.-Y., Eds. John Wiley & Sons, Inc.: Hoboken, NJ, 2015; pp 1-100.

13. Kumar, B.; Kaushik, B. K.; Negi, Y. S., Organic Thin Film Transistors: Structures, Models, Materials, Fabrication and Applications: A Review. *Polym. Rev.* **2014,** *54* (1), 33-111.

14. Zhou, K.; Dong, H.; Zhang, H.; Hu, W., High Performance n-type and Ambipolar Small Organic Semiconductors for Organic Thin Film Transistors. *Phys. Chem. Chem. Phys.* **2014,** *2014*, 22448-22457.

15. Kumavat, P. P.; Sonar, P.; Dalal, D. S., An Overview on Basics of Organic and Dye Sensitized Solar Cells, Their Mechanism and Recent Improvements. *Renew. Sust. Energ. Rev.* **2017,** *78*, 1262-1287.

16. Mishra, A.; Bäuerle, P., Small Molecule Organic Semiconductors on the Move: Promises for Future Solar Energy Technology. *Angew. Chem. Int. Ed.* **2012,** *51* (9), 2020-2067.

17. Mazzio, K. A.; Luscombe, C. K., The Future of Organic Photovoltaics. *Chem. Soc. Rev.* **2015,** *44*, 78-90.

18. Kippelen, B.; Brédas, J. L., Organic Photovoltaics. *Energy Environ, Sci.* **2009,** *2*, 251-261.

19. Zhang, C.; Chen, P.; Hu, W., Organic Light-Emitting Transistors: Materials, Device Configurations and Operations. *Small* **2016,** *12* (10), 1252-1294.

20. Yook, K. S.; Lee, J. Y., Small Molecule Host Materials for Solution Processsed Phosporescent Organic Light-Emitting Diodes. *Adv. Mater.* **2014,** *26* (25), 4218-4233.

21. Reineke, S., Complementary LED Technologies. *Nature Materials* **2015,** *14* (5), 459-462.

22. Fraboni, B.; Fraleoni-Morgera, A.; Geerts, Y.; Morpurgo, A. F.; Podzorov, V., Organic Single Crystal: An Essential Step to New Physics and Higher Performances of Optoelectronic Devices. *Adv. Funct. Mater.* **2016,** *26*, 2229-2232.

23. Reese, C.; Bao, Z., Organic Single-crystal Field-effect Transistors *Mater. Today* **2007,** *10*, 20-27.

24. Podzorov, V., Organic Single Crystals: Addressing the Fundamentals of Organic Electronics. *MRS Bull.* **2013,** *38*, 15-24.

25. Xie, W. X.; Menke, S. M.; Frisbie, C. D.; Holmes, R. J., Experimental Characterization of Charge and Exciton Transport in Organic Semiconductors. In *The WSPC Reference on Organic Electronics: Organic Semiconductors*, Brédas, J. L.;

Marder, S. R.; André, J.-M., Eds. World Scientific Publishing Co. Pte. Ltd.: Singapore, 2016; Vol. 1, pp 231-291.

26. Takimiya, K.; Nakano, M.; Sugino, H.; Osaka, I., Design and Elaboration of Organic Molecules for High Field-Effect-Mobility Semiconductors. *Syn. Metals* **2016,** *217*, 68-68.

27. Shi, X.; Chi, C., Different Strategies for the Stabilization of Acenes and Acene Analogues. *Chem. Rec.* **2016,** *16*, 1690-1700.

28. McGarry, K. A.; Xie, W.; Sutton, C.; Risko, C.; Wu, Y.; Young Jr., V. G.; Brédas, J. L.; Frisbie, C. D.; Douglas, C. J., Rubrene-Based Single-Crystal Organic Semiconductors: Synthesis, Electronic Structure, and Charge-Transport Properties. *Chem. Mater.* **2013,** *25*, 2254-2263.

29. Coropceani, V.; Cornil, J.; da Silva Filho, D. A.; Oliver, Y.; Silbey, R. J.; Brédas, J. L., Charge Transport in Organic Semiconductors. *Chem. Rev.* **2007,** *107*, 926-952.

30. Schweicher, G.; Olivier, Y.; Lemauer, V.; Geerts, Y. H., What Currently Limits Charge Carrier Mobility in Crystals of Molecular Semiconductors. *Isr. J. Chem.* **2014,** *54*, 595-620.

31. Anthony, J. E., The Larger Acenes: Versatile Organic Semiconductors. *Angew. Chem. Int. Ed.* **2008,** *47*, 452-483.

32. Anthony, J. E., Functionalized Acenes and Heteroacenes for Organic Electronics. *Chem. Rev.* **2006,** *106*, 5028-5048.

33. Farchioni, R.; Grosso, G., *Organic Electronic Materials Conjugated Polymeers and Low Molecular Weight Organic Solids*. Springer-Verlag: New York, 2001.

34. Facchetti, A., π-Conjugated Polymers for Organic Electronics and Photovoltaic Cell Applications. *Chem. Mater.* **2010,** *23* (3), 733-758.

35. Pundsack, T. J.; Haugen, N. O.; Johnstone, L. R.; Frisbie, C. D.; Lidberg, R. L., Temperature Dependent **c**-axis Hole Mobilities in Rubrene Single Crystals Determined by Time-of-Flight. *Appl. Phys. Lett.* **2015,** *106* (11), 113301.

36. Xia, Y.; Kalihari, V.; Frisbie, C. D.; Oh, N. K.; Rogers, J. A., Tetracene Air-Gap Single-Crystal Field-Effect Transistors *Appl. Phys. Lett.* **2007,** *90*, 162106.

37. Ostroverkhova, O.; Cooke, D. G.; Hegmann, F. A.; Anthony, J. E.; Podzorov, V.; Gershensom, M.; Jurchescu, O. D.; Palsta, T. T. M., Ultrafast Carrier Dynamics in Pentacene, Functionalized Pentacene, Tetracene and Rubrene Single Crytstals. *Appl. Phys. Lett.* **2006,** *88*, 162101.

38. Podzorov, V.; Menard, E.; Borissov, A.; Kiryukhin, V.; Rogers, J.; Gershensom, M., Intrinsic Charge Transport on the Surface of Organic Semiconductors *Phys. Rev. Lett.* **2004,** *93* (8), 086602.

39. de Boer, R. W. I.; Klapwijk, T. M.; Morpurgo, A. F., Field-Effect Transistors on Tetracene Single Crystals *Appl. Phys. Lett.* **2003,** *83* (21), 4345-4347.

40. Butko, V. Y.; Chi, X.; Lang, D. V.; Ramirez, A. P., Field-Effect Transitor on Pentacene Single Crystal. *Appl. Phys. Lett.* **2003,** *83* (23), 4773-4775.

41. Fleming, I., *Molecular Orbitals and Organic Chemical Reactions*. John Wiley and Sons Ltd.: West Sussex, UK, 2009.

42. Brütting, W., Introduction to the Physics of Organic Semiconductors. In *Physics of Organic Semiconductors*, Brütting, W., Ed. Wiley-VCH: Weinheim, 2005; pp 1-14.

43. Prasad, S.; Ifraz, M.; Prasad, R.; Deen, Z.-U. Atomic Orbital & Bonding: Sigma (σ) & Pi (π) Bonds. https://sites.google.com/site/ed350201003/home.

44. Bredas, J. L.; Calbert, J. P.; da Silva Filho, D. A.; Cornil, J., Organic Semiconductors: A Theoretical Characterization of the Basic Parameters Governing Charge Transport *P Natl. Acad. Sci. USA* **2002,** *99* (9), 5804-5909.

45. Turro, N. J., *Modern Molecular Photochemistry*. University Science Books: Sausalito, CA, 1991.

46. Harrison, W. A., *Electronic Structure and the Properties of Solids: The Physics of the Chemical Bond*. Dover Publicaations, Onc.: New York, 1989.

47. Roncali, J., Molecular Engineering of the Band Gap of π-Conjugated Systems: Facing Technological Applications. *Macromol. Rapid Commun.* **2007,** *28*, 1761-1775.

48. da Silva Filho, D. A.; Kim, E.-G.; Brédas, J. L., Transport Properties in the Rubrene Crystal: Electronic Coupling and Vibrational Reorganization Energy *Adv. Mater.* **2005,** *17* (8), 1072-1076.

49. Ferendeci, *Physical Foundations of Solid State and Electron Devices*. McGraw-Hill, Inc.: New York, 1991.

50. Hummel, R. E., *Electronic Propeties of Materials*. Springer: New York, 2001.

51. Cheng, Y. C.; Silbey, R. J.; da Silva Filho, D. A.; Calbert, J. P.; Brédas, J. L., Three-Dimensional Band Structure and Bandlike Mobility in Oligocene Single Crystal: A Theoretical Investigation. *J.Chem. Phys.* **2003** *118* (8), 3764-3774.

52. Li, Y.; Coropceanu, V.; Brédas, J. L., Thermal Narrowing of the Electronic Bandwidths in Organic Molecular Semiconductors: Impact of the Crystal Thermal Expansion. *J. Phys. Chem. Lett.* **2012,** *3*, 3325-3329.

53. Jurschescu, O. D.; Meetsma, A.; Palsta, T. T. M., Low-Temperature Structure of Rubrene Single Crystals Grown by Vapor Transport *Acta Crystallogr. B* **2006** *B62*, 330-334.

54. Ashcroft, N. W.; Merim, N. D., *Solid State Physics*. Thomson Learning, Inc.: Stamford, CT, 1976.

55. Singleton, J., *Band Theory and Electronic Properties of Solids*. Oxford University Press: New York, 2001.

56. Merthe, D. How does quantum mechanics describe electrical conductivity? https://www.quora.com/How-does-quantum-mechanics-describe-electrical-conductivity.

57. Solymar, L.; Walsh, D., *Lectures on the Electrical Properties of Materials*. Oxford University Press: New York, 1993.

58. Ling, M.-M.; Reese, C.; Briseno, A. L.; Bao, Z., Non-Destructive Probing of the Anistropy of Field-Effect Mobility in the Rubrene Single Crystal. *Synthetic Met.* **2007,** *157* (6-7), 257-260.

59. Gershenson, M. E.; Podzorov, V.; Morpurgo, A. F., Colloquium: Electronic Transport in Single-Crystal Organic Transistors *Rev. Mod. Phys.* **2006,** *78* (3), 973-989.

60. Moraski, H.; Koretsune, T.; Hotta, C.; Takeya, J.; Kimura, T.; Wakabayashi, Y., Large Surface Relaxation in the Organic Semiconductor Tetracene. *Nat. Comm.* **2014,** *5*, 5400.

61. Lundstrom, M., *Fundamentals of Carrier Transport*. 2nd ed.; Cambridge University Press: New York, 2000.

62. Marcus, R. A., On the Theory of Oxidation-Reduxtion Reactions Involving Electron transfer I. *J. Chem. Phys.* **1956,** *24* (5), 966-978.

63. Marcus, R. A., Electron Transfer Reactions in Chemistry. Theory and Experiment. *Rev. Mod. Phys.* **1993,** *65* (3), 599-610.

64. Holstein, T., Studies of Polaron Motion: Part I. The Molecular-Crystal Model *Ann. Phys.* **1959,** *8*, 325-342.

65. Holstein, T., Studies of Polaron Motion: Part II. The Small Polaron *Ann. Phys.* **1959** *8*,343-389.

66. Karl, N., Charge Carrier Transport in Organic Semiconductors. *Syn. Metals* **2003,** *133-134*, 649-657.

67. Troisi, A., Charge Transport in High Mobility Molecular Semiconductors: Classical Models and New Theories. *Chem. Soc. Rev.* **2011,** *40*, 2347-2358.

68. Bässler, H.; Köhler, A., Charge Transport in Organic Semiconductors. *Top. Curr. Chem.* **2012,** *312*, 1-65.

69. Fratini, S.; Ciuchi, S., Bandlike Motion and Mobility Saturation in Organic Molecular Semiconductors. *Phys. Rev. Lett.* **2009,** *103*, 266601.

70. Ishii, H.; Honma, K.; Kobayashi, N.; Hirose, K., Wave-packet Approach to Transport Properties of Carrier Couplesd with Intermolecular and Intramolecualr Vibrations of Organic Semiconductors. *Phys. Rev. B* **2012,** *85* (24), 245206.

71. Fratini, S.; Mayou, D.; Ciuchi, S., The Transient Localization Scenario for Charge Transport in Crystalline Organic Materials *Adv. Funct. Mater.* **2015,** *26* (14), 2292–2315.

72. Troisi, A.; Orlandi, G., Charge-Transport Regime of Crystalline Organic Semiconductors: Diffusion Limited by Thermal off-Diagonal Electronic Disorder *Phys. Rev. Lett.* **2006,** *96* (8), 086601.

73. Blülle, B.; Troisi, A.; Häusermann, R.; Batlogg, B., Charge Transport Perpendicular to the High Mobility Plane in Organic Crystals: Bandlike Temperature Dependence Maintained Despite Hundredfold Anisotropy *Phys. Rev. B* **2016,** *9* (3), 035205.

74. Sirringhaus, H.; Sakanoue, T.; Chang, J.-F., Charge-Transport Physics of High-Mobility Molecular Semiconductors *Phys. Status Solidi B* **2012** *9*,1655-1676.

75. Troisi, A., Theories of the Charge Transport Mechanism in Ordered Organic Semiconductors *Adv. Polym. Sci.* **2010,** *223*, 259-300.

76. Peierls, R. E., *Quantum Theory Of Solids*. Oxford Univerisyt Press: New York, 2001.

77. Martinelli, N. G.; Idé, J.; Sánchez-Carrera, R. S.; Coropceanu, V.; Brédas, J. L.; Ducasse, L.; Castet, F.; Cornil, J.; Beljonne, D., Influence of Structural Dynamic on Polarization Energies in Anthracene Single Crystals *J. Phys. Chem.* **2010,** *114* (48), 20678-20685.

78. Li, Y.; Coropceani, V.; Brédas, J.-L., Charge Transport in Crystalline Organic Semiconductors. In *The WSPC Reference on Organic Electronics: Organic Semiconductors*, Brédas, J.-L.; Marder, S. R., Eds. World Scientific Publishing Co. Pte. Ltd.: Singapore, 2016; Vol. 1, pp 193-230.

79. McMahon, D. P.; Troisi, A., Evaluation of the External Reorganization Energy of Polyacenes. *J. Phys. Chem. Lett.* **2010,** *1*, 941-946.

80. Brëdas, J. L.; Beljonne, D.; Coropceani, V.; Cornil, J., Charge-Transfer and Energy-Transfer Processes in π-Conjugated Oligmers and Polymers: A Molecular Picture. *Chem. Rev.* **2004,** *104* (11), 4971-5004.

81. Heeger, A. J.; Kivelson, S.; Schrieffer, J. R.; Su, W.-P., Solitons in Conducting Polymers. *Rev. Mod. Phys.* **1988,** *60* (3), 781-851.

82. Troisi, A.; Orlandi, G., Dynamics of the Intermolecular Transfer Integral in Crytsalline Organic Semiconductors. *J. Phys. Chem.* **2006,** *110*, 4065-4070.

83. Silinsh, E. A.; Klimkāns, A.; Larsson, S.; Čápek, V., Molecular Polaron States in Polyacene Crystals. Formation and Transfer Processes. *Chem. Phys.* **1995,** *198* (3), 311-331.

84. Emin, D., Optical Properties of Large and Small Polarons and Bipolarons. *Phys. Rev. B* **1993,** *48* (18), 13691-13702.

85. Tamura, H.; Tsukada, M.; Ishii, H.; Kobayashi, N.; Hirose, K., Roles of Intramolecular and Intermolecular Electron-Phonon Coupling on the Formation and Transport of Large Polarons in Organic Semiconductors. *Phys. Rev. B* **2012,** *86*, 035208.

86. Hannewald, K.; Stojanović, V. M.; Schellekens, J. M. T.; Bobbert, P. A.; Kresse, G.; Hafner, J., Theory of Polaron Bandwidth Narrowing in Organic Molecular Crystals. *Phys. Rev. B* **2004,** *69*, 075211.

87. Troisi, A.; Orlandi, G.; Anthony, J. E., Electronic Interactions and Thermal Disorder in Molecular Crystals Containing Cofacial Pentacene Units. *Chem. Mater.* **2005,** *17*, 5024-5031.

88. Coropceanu, V.; Malagoli, M.; da Silva Filho, D. A.; Gruhn, N. E.; Bill, T. G.; Brédas, J. L., Hole-and Electron-Vibrational Couplings in Oligoacene Crystals: Intramolecular Contributions *Phys. Rev. Lett.* **2002,** *89* (27), 275503.

89. Girlando, A.; Grisanti, L.; Masino, M., Peierls and Holstein Carrier-Phonon Coupling in Crystallin Rubrene. *Phys. Rev. B* **2010,** *82*, 035208.

90. Malagoli, M.; Brédas, J. L., Density Functional Theory Study of the Geometric Structure and Energetics of Triphenylamine-Based Hole-Transporting Molecules. *Chem. Phys. Lett.* **2000,** *327*, 13-17.

91. Malagoli, M.; Coropceani, V.; da Silva Filho, D. A.; Brédas, J. L., A Multimode Analysis of the Gas-Phase Photoelectron Spectra in Oligoacenes. *J. Chem. Phys.* **2004,** *120* (16), 7490-7496.

92. Gunnarsson, O.; Calandra, M.; Han, J. E., Saturation of Electrical Resistivity. *Rev. Mod. Phys.* **2003,** *75* (4), 1085-1099.

93. Madhukar, A.; Post, W., Exact Solution for the Diffusion of a Particle in a Medium with Site Diagonal and Off-Diagonal Dynamic Disorder. *Phys. Rev. Lett.* **1977,** *39* (22), 1424-1427.

94. Gosar, P.; Choi, S.-I., Linear-Response Theory of the Electron Mobility in Molecular Crystals. *Phys. Rev.* **1966,** *150* (2), 529-538.

95. Ren, X.; Bruzek, M. J.; Hanfi, D. A.; Schulzetenberg, A.; Wu, Y.; Kim, C.-H.; Zhang, Z.; Johns, J. E.; Salleo, A.; Fratini, S.; Troisi, A.; Douglas, C. J.; Frisbie, C. D., Negative Isotope Effect on Field-Effect Hole transport in Fully Substituted ^{13}C-Rubrene. *Adv. Electron. Mater.* **2017,** *3* (4), 1700018

96. Yada, H.; Uchida, R.; Sekine, H.; Terashige, T.; Tao, S.; Matsui, Y.; Kida, N.; Fratini, S.; Ciuchi, S.; Okada, Y.; Uemura, T.; Takeya, J.; Okamoto, H., Carrier Dynamics of Rubrene Single-Crystals Revealed by Transient Broadband Tetrahertz Spectroscopy. *Appl. Phys. Lett.* **2014,** *105* (14), 143302.

97. Minder, N. A.; Lu, S.; Fratini, S.; Ciuchi, S.; Facchetti, A.; Morpurgo, A. F., Tailoring the Molecular Structure to Suppress Extrinsic Disorder in Organic Transistors. *Adv. Mater.* **2014,** *26* (8), 1254-1260.

98. Eggeman, A. S.; Illig, S.; Troisi, A.; Sirringhaus, H.; Midgley, P. A., Measurement of Molecular Motion in Organic Semiconductors by Thermal Diffuse Electron Scattering. *Nat. Mater.* **2013,** *12* (11), 1045-1049.

99. Troisi, A., Prediction of the Absolute Charge Mobility of Molecular Semiconductors: The Case of Rubrene *Adv. Mater.* **2007,** *19* (15), 2000-2004.

100. Kokil, A.; Yang, K.; Kumar, J., Techniques for Characterization of Charge Carrier Mobility in Organic Semiconductors. *J. Polym. Sci. Pol. Phys.* **2012,** *50*, 1130-1144.

101. Tessler, N., Experimental Techniques and the Underlying Device Physics. *J. Polym. Sci. Pol. Phys.* **2014,** *52*, 1119-1152.

102. Tiwari, S.; Greenham, N. C., Charge Mobility Measurements Techniques in Organic Semioconductors. *Opt. Quant. Electron.* **2009,** *41*, 69-89.

103. Spear, W. E., Transit Time Measurements of Charge Carriers in Amorphous Selenium Films. *Proc. Phy. Soc. B* **1957,** *70* (7), 669-675.

104. Spear, W. E., The Hole Mobility in Selenium. *P. Phys. Soc.* **1960,** *70* (6), 826-832.

105. Kepler, Charge Carrier Production and Mobility in Anthracene Crystals. *Phys. Rev.* **1960,** *119* (4), 1226-1229.

106. LeBlanc, O. H., Hole and Electron Drift Mobilities in Anthracene. *J. Chem. Phys.* **1960,** *33*, 626.

107. Warta, W.; Stehle, R.; Karl, N., Ultrapure, High Mobility Organic Photoconductors. *Appl. Phys. A.* **1985,** *36*, 163-170.

108. Karl, N.; Marktanner, J.; Stehle, R.; Warta, W., High-Field Saturation of Charge Carrier Drift Velocities in Ultrapurified Organic Photoconductors. *Synthetic Met.* **1991,** *41-43*, 2473-2481.

109. Karl, N.; Marktanner, J., Electron and Hole Mobilities in High Purity Anthracene Single Crystals. *Mol. Cryst. Liq. Crys. A* **2001,** *355* (1), 149-173.

110. Liu, S.-W.; Lee, C.-C.; Su, W.-C.; Yuan, C.-H.; Lin, C.-F.; Chen, K.-T.; Shu, Y.-S.; Li, Y.-Z.; Su, T.-H.; Huang, B.-Y.; Chang, W.-C.; Liu, Y.-H., Downscaling the Sample Thickness to Sub-Micrometers by Employing Organic Photovoltaic Materials as a Charge-Generation Layer in the Time-of-Flight Measurement. *Sci. Rep.* **2015,** *5*, 10384.

111. Spear, W. E., Drift Mobility Techniqies for the Study of Electrical Transport Properties in Insulating Solids. *J. Non-Cryst. Solids* **1969,** *1*, 194-214.

112. Scher, H.; Montroll, E. W., Anomalous Transit-Time Dispersion in Amorphous Solids. *Phys. Rev. B* **1975,** *12* (6), 2455-2477.

113. Kikuchi, Y.; Wakamatsu, T.; Takahashi, H.; Endo, I., Analysis of TOF Transient Currents Affected by Circuit Time Constants *Electr. Eng. Jpn.* **2003** *143*, 1-7.

114. Pope, M.; Swenberg, C. E., *Electronic Processes in Organic Crystals and Polymers*. 2nd ed.; Oxford University Press: New York, 1999.

115. Karl, N., Charge-Carrier Mobility in Organic Crystals. In *Organic Electronic Materials Conjugated Polymers and Low Molecular Weight Organic Solids*, Farchoni, R.; Grosso, G., Eds. Springer-Verlag: New York, 2001; pp 283-326.

116. Borsenberger, P. M.; Bassler, H., Tail Broadening of Photocurrent Transients in Molecularly Doped Polymers. *J. Appl. Phys.* **1994,** *75* (2), 967-972.

117. Shockley, W.; Read, W. T., Statistics of the Recombinations of Holes and Electrons. *Phys. Rev.* **1952,** *87* (5), 835-842.

118. Dodabalapur, A.; Torsi, L.; Katz, H. E., Organic Transistors: Two-Dimensional Transport and Improved Electrical Characteristics. *Science* **1995,** *268*, 270-271.

119. Isberg, J.; Majdi, S.; Gabrysch, M.; Friel, I.; Balmer, R. S., A Lateral Time-of-Flight System for Charge Transport Studies. *Diam. Relat. Mater.* **2009,** *18*, 1163-1166.

120. Kovi, K. K.; Majdi, S.; Gabrysch, M.; Isberg, J., A Charge Transport Study in Diamond, Surface Passivated by High-k Dielectric Oxides. *Appl. Phys. Lett.* **2014,** *105*, 202102.

121. Kitamura, M.; Imada, T.; Kako, S.; Arakawa, Y., Time-of-Flight Measurement of Lateral Carrier Mobility in Organic Thin Films. *Jpn. J. Appl. Phys.* **2004,** *43* (4B), 2326-2329.

122. Kuwahara, A.; Naka, S.; Okada, H.; Onnagawa, H., Carrier Mobility of Organic Thin Films Using Lateral Electrode Structure with Optical Slits. *Appl. Phys. Lett.* **2006,** *89*, 132106.

123. Kougo, J.; Ishikawa, K., Evaluation of Anisotropic Charge Carrier Mobility of Perylene Single Crystals by Time-of-Flight Method. *Jpn. J. Appl. Phys.* **2016,** *55*, 030304.

124. Kim, C.-H.; Bonnassieux, Y.; Horowitz, G., Compact DC Modeling of Organic Field-Effect Transistors: Review and Perspectives. *IEEE T. Electron. Dev.* **2014,** *61* (2), 278-287.

125. Zaumseil, J.; Sirringhaus, H., Electron and Ambipolar Transport in Organic Field-Effect Transistors. *Chem. Rev.* **2007,** *107* (4), 1296-1323.

126. Choi, D.; Chu, P.-H.; McBride, M.; Reichmanis, E., Best Practices for Reporting Organic Field Effect Transistor Device Performance. *Chem. Mater.* **2015,** *27*, 4167-4168.

127. Laudise, R. A.; Kloc, C.; Simpkins, P. G.; Siegrist, T., Physical Vapor Growth of Organic Semiconductors. *J Cryst. Growth* **1998,** *187*, 449-454.

128. Niemax, J.; Tripathi, A. K.; Pflaum, J., Comparison of the Electronic Properties of Sublimation and Bridgeman Grown Crystals of Tetracene. *Appl. Phys. Lett.* **2005,** *86*, 122105.

129. Vrijmoeth, J.; Stok, R. W.; Veldman, R.; Schoonveld, W. A.; Klapwijk, T. M., Single Crystallites in Planar Polycrystalline Oligothiophene Films: Determination of Orientation and Thickness by Polarization Microscopy. *J. Appl. Phys.* **1998,** *83* (7), 3816-3824.

130. Irkhin, P.; Ryasnyanskiy, A.; Koehler, M.; Biaggio, I., Absorption and Photoluminescence Spectroscopy of Rubrene Single Crystals. *Phys. Rev. B* **2012,** *86*, 085143.

131. Niemax, J.; Tripathi, A. K.; Pflaum, J., Comparison of the Electronic Properties of Sublimation and Vapor Bridgman Grown Crystals of Tetracene *Appl. Phys. Lett.* **2005,** *86*, 122105.

132. de Boer, R. W. I.; Jochemsen, M.; Klapwijk, T. M.; Morpurgo, A. F., Space Charge Limited Transport and Time of Flight Measurements in Tetracene Single Crystals: A Comparative Study *J. Appl. Phys.* **2004,** *95* (3), 1196-1202.

133. Berrehar, J.; Delannoy, P.; Schott, M., Drift Mobility of Holes in Crystalline Tetracene *Phys. Status Solidi B* **1976,** *77*, K119-K122.

134. Wu, Y.; Ren, X.; McGarry, K. A.; Bruzek, M. J.; Douglas, C. J.; Frisbie, C. D., Scanning Kelvin Probe Microscopy Reveals Planar Defects Are Sources of Electronic Disorder in Organic Semiconductor Crystals. *Adv. Electron. Mater.* **2017,** *3* (7), 1700117.

135. Ling, M.-M.; Reese, C.; Briseno, A. L.; Bao, Z., Non-Destructive Probing of the Anistropy of Field-Effect Mobility in the Rubrene Single Crystal *Synthetic Met.* **2007,** *157* (6-7), 257-260.

136. Williams, W., Hole Mobility in Rubrene *Discuss. Faraday Soc.* **1971,** *51*, 61-66.

137. Geacintov, N.; Pope, M.; Kalmann, H., Photogeneration of Charge Carriers in Tetracene. *J. Chem. Phys.* **1966,** *45* (7), 2639-2649.

138. Obarowska, M.; Signerski, R.; Godlewski, J., Generation of Charge Carrier Pairs in Tetracene Layers *Macromol. Symp.* **2004,** *212*, 427-433.

139. Goldmann, C.; Haas, S.; Krellner, C.; Pernstich, K. P.; Gundlach, D. J., Hole Mobility in Organic Single Crystals by a "Flip-Crystal" Field-Effect Technique *J. Appl. Phys.* **2004,** *98* (4), 2080-2086